Technische Universität München

Fakultät Chemie

Lehrstuhl für Technische Elektrochemie

# Neutron-based investigation of aging aspects of the intrinsically safe cathode material $LiFe_xMn_{1-x}PO_4$

Dissertation

Benjamin Starke

TECHNISCHE UNIVERSITÄT MÜNCHEN

Fakultät Chemie

Lehrstuhl für Technische Elektrochemie

# Neutron-based investigation of aging aspects of the intrinsically safe cathode material $LiFe_xMn_{1-x}PO_4$

Benjamin Starke

Vollständiger Abdruck der von der Fakultät für Chemie der Technischen Universität München zur Erlangung des akademischen Grades eines

Doktors der Naturwissenschaften (Dr. rer. nat.)

genehmigten Dissertation.

| | | |
|---|---|---|
| Vorsitzender: | | Prof. Dr. Tom Nilges |
| Prüfer der Dissertation | 1. | Prof. Dr. Hubert A. Gasteiger |
| | 2. | Prof. Dr. Karl-Heinz Pettinger |

Die Dissertation wurde am 02.07.2018 bei der Technischen Universität München eingereicht und durch die Fakultät für Chemie am 30.11.2018 angenommen.

# Abstract

Nowadays lithium-ion batteries are in use for various mobile and stationary applications. With increasing dissemination, aspects of operational safety of batteries become a key issue. Regular reports on safety-critical incidents prove the need for action in the field of battery safety. One possibility to improve the operational safety of lithium-ion batteries is the application of intrinsically safe cathode active materials. Phosphate-type materials like $LiFe_xMn_{1-x}PO_4$ are an alternative to the nowadays commonly used oxide-type cathode materials.

The objective of this publication-based dissertation is the investigation of aging mechanisms associated with $LiFe_xMn_{1-x}PO_4$. The work is focused on aging effects related to different material storage conditions, material morphologies, variations in processing as well as structural deficits and their influence on the electrochemical performance and long-term characteristics. All publications contain results from neutron-based experiments.

In the first publication different morphologies of $LiFePO_4$ and their influence on water- and solvent-based slurry processing are investigated. The effect of particle morphology on electrochemical properties was studied with a focus on different (dis-)charge behavior and long-term capacity retention.

The second publication investigates the effect of different detrimental storage conditions of $LiFe_xMn_{1-x}PO_4$ on changes of material properties. Water- and solvent-based processing of pristine and aged samples as well as electrochemical characterization allowed the evaluation of potentially cumulative aging effects as a result of material storage and subsequent processing.

In the third publication *in-operando* neutron imaging is applied to quantify the different initial gas evolution in $LiFePO_4$/graphite and $LiFe_xMn_{1-x}$PO4/graphite cells. The long-term evolution of Mn-dissolution and subsequent migration to the graphite anode was studied via Prompt Gamma Activation Analysis. The results allow a direct comparison with the Mn-dissolution occurring in oxide-type cathode active materials.

# Zusammenfassung

Heutzutage werden Lithium-Ionen Batterien in zahlreichen mobilen und stationären Anwendungen eingesetzt. Mit steigender Verbreitung muss dabei dem Aspekt der operativen Sicherheit zunehmende Bedeutung beigemessen werden. Regelmäßige sicherheitskritische Zwischenfälle bestätigen, dass im Bereich der Batteriesicherheit nach wie vor Handlungsbedarf besteht. Eine Möglichkeit, die Sicherheit von Lithium-Ionen-Batterien zu verbessern, kann unter anderem durch den Einsatz eigensicherer Kathodenmaterialien erreicht werden. Als Ersatz für heute übliche Oxidverbindungen bieten sich dabei Phosphatverbindungen wie $LiFe_xMn_{1-x}PO_4$ an.

Ziel dieser publikationsbasierten Dissertation ist es, neue mit $LiFe_xMn_{1-x}PO_4$ assoziierte Alterungsmechanismen aufzuklären. Dabei liegt der Fokus auf dem Einfluss von Lagerungsbedingungen, Materialmorphologie, Verarbeitungsprozessen und struktureller Defizite des Materials auf das elektrochemische Leistungs- und Langzeitverhalten. Alle Publikationen enthalten dabei Ergebnisse die mit neutronenbasierten Experimenten gewonnen wurden.

In der ersten Publikation wird der Einfluss verschiedener $LiFePO_4$ Materialmorphologien auf die wasser- und lösemittelbasierte Verarbeitung untersucht, sowie deren Effekt auf das Ladeverhalten und die Langzeitzyklisierung.

Die zweite Publikation beschäftigt sich mit den Folgen verschiedener, schädlicher Lagerungsbedingungen des Ausgangmaterials und den damit verbundenen Eigenschaftsänderungen. Die anschließende wasser- und lösemittelbasierte Weiterverarbeitung des frischen und gealterten Ausgangsmaterials sowie deren elektrochemische Charakterisierung liefern Ergebnisse zu eventuellen kumulativen Alterungseffekten.

In der dritten Publikation wird mittels *in-operando* Neutronenradiographie der Einfluss der Manganauflösung aus $LiFe_xMn_{1-x}PO_4$ auf die initiale Gasentwicklung in der Zelle untersucht, und dabei mit dem manganfreien $LiFePO_4$ verglichen. Die Langzeitentwicklung der Manganauflösung und die Migration von Mangan-Ionen zur Anode wird mittels Prompter Gamma Aktivierungsanalyse quantifiziert. Die Ergebnisse ermöglichen einen Vergleich mit der bei oxidbasierten Kathodenmaterialen ebenfalls auftretenden Manganauflösung.

# List of Abbreviations

APU - Auxiliary Power Unit

CCD - Charge-Coupled Device

CMC - Carboxymethyl Cellulose

EDX - Energy Dispersive X-ray Spectroscopy

FRM II - Forschungsreaktor München II

hcp - hexagonal close packing

ICL - Irreversible Capacity Loss

ICP-OES - Inductively Coupled Plasma Optical Emission Spectrometry

NCA - $LiNiCoAlO_2$ / $LiNi_xCo_yAl_{1-x-y}O_2$

LCO - $LiCoO_2$

LFP - $LiFePO_4$

LFMP - $LiFeMnPO_4$ / $LiFe_xMn_{1-x}PO_4$

LMNO - $LiMnNiO_4$ / $LiMn_{2-x}Ni_xO_4$

LTO - $Li_4Ti_5O_{12}$

MLZ - Heinz Maier-Leibnitz Zentrum

ND - Neutron Diffraction

NI - Neutron Imaging

NR - Neutron Radiography

NMC - $LiNiMnCoO_2$ / $LiNi_xMn_yCo_{1-x-y}O_2$

NMP - N-methyl-2-pyrrolidone

PAS - Positron Annihilation Spectroscopy

PGAA - Prompt Gamma Activation Analysis

PP - Primary Particle

rh - relative humidity

SA - Secondary Agglomerate

SBR - Styrene-Butadiene Rubber

SEI - Solid Electrolyte Interface

SOC - State of Charge

XRD - X-ray diffraction

# Table of Contents

# 1. Introduction

This section provides an introductory overview of safety issues related to lithium-ion batteries, information on the cathode active material $LiFe_xMn_{1-x}PO_4$, describes its electrochemical properties and applications and outlines previous research results in the context of aging phenomena. Since neutron-based analytical methods have been applied in this project, the distinct advantages of neutrons and aspects of the application of neutron research on lithium-ion batteries will be introduced. Instruments at the Forschungsreaktor München II (FRM II) which were used for experiments in the scope of this thesis are described at the end of this section.

## 1.1. Safety aspects of lithium-ion batteries

The concept of reversible intercalation of lithium-ions into host structures has first been described by Armand in 1980 [1, 2]. His idea led to the development and investigation of different intercalation materials and spinel-type transition metal oxides appeared to be suitable for application as cathode materials [3, 4]. After overcoming the problems of co-intercalation of electrolyte molecules, graphite had been identified as an appropriate anode material [5, 6]. Being intensively involved in their development, SONY brought the first commercial lithium-ion batteries on the market in 1991 [7]. At this time, aqueous batteries systems like NiCd and NiMH with a cell voltage limited to 1.5 V were commonly used [8]. But the newly introduced lithium-ion batteries used non-aqueous electrolytes allowing a significantly higher cell voltage of 4.1 V [9]. The resulting higher energy density was of special importance for mobile applications [10].

More than 25 years after the market launch of lithium-ion batteries, layered transition metal oxides and graphite are the most commonly applied cathode and anode materials, respectively [11]. Besides the beneficial high voltage and energy density, several safety concerns are arising from materials used in lithium-ion batteries. The various chemical processes in an operating lithium-ion battery and their interaction are very complex. Thus, only some safety-related issues will be discussed in this section.

A fundamental problem of layered transition metal oxides like $LiCoO_2$ (LCO) is the increasing instability in the de-lithiated state and at temperatures above 200 °C it disproportionates into oxygen and other degradation compounds. This means that in case of a battery fire the cathode material itself reinforces heat generation. The described self-reinforcing process is called thermal runaway and occurs when the heat generation exceeds heat dissipation [12, 13].

In detail, a thermal runaway always has an initial trigger, which can for example be mechanical, thermal or electrical stress like battery penetration/compression, overheating or overcharging, respectively. Subsequently, energy is released as the negative electrode reacts with the electrolyte. At increasing temperature, the cathode material starts to react with the electrolyte, causing a further increase of temperature and electrolyte decomposition. In the next step, the positive electrode material decomposes. At this point the thermal runaway can no longer be stopped, since oxygen is released from the material itself and no external source of oxygen is required to maintain the thermal runaway. This applies in particular when transition metal oxides like $LiCoO_2$ are used as cathode materials. An exemplary reaction of $LiCoO_2$ with the electrolyte is described below [14–16]:

$$10\ Li_{0.5}CoO_2 + C_3H_4O_3 \rightarrow 5\ LiCoO_2 + 5\ CoO + 3\ CO_2 + 2\ H_2O \qquad (1)$$

As indicated in equation (1) the reactivity of $LiCoO_2$ is given and elevated by partial de-lithiation (*e. g.* $Li_{0.5}CoO_2$). Irreversible thermal runaway and oxygen release is obtained at further temperature increase due to lattice collapse of partially de-lithiated $Li_{0.5}CoO_2$ [14]:

$$6\ Li_{0.5}CoO_2 \rightarrow 3\ LiCoO_2 + Co_3O_4 + O_2 \qquad (2)$$

The risk of oxygen and energy release as described in equation (2) applies also for other transition metal oxides as depicted in Figure 1.

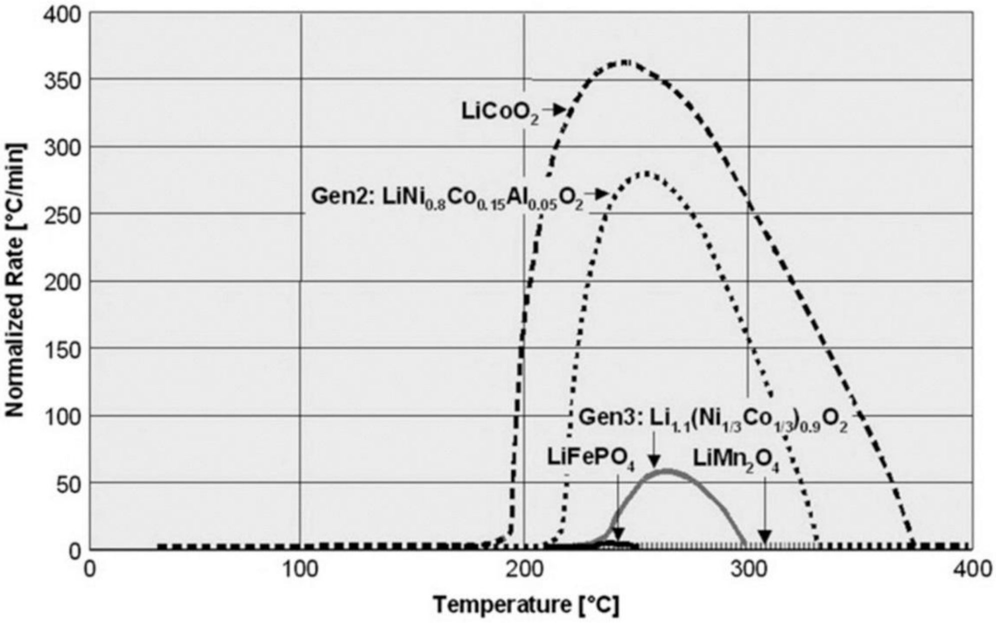

Figure 1: Extent and initial temperature of energy release of different cathode active materials. Reproduced from reference [15] with permission from Springer Nature.

As illustrated in Figure 1, energy release differs significantly for different cathode materials and is highest for $LiCoO_2$. Compared to $LiCoO_2$, the observable energy release of second (*e. g.* $LiNi_{0.8}Co_{0.15}Al_{0.05}O_2$) and third generation oxide-type materials (*e. g.* $Li_{1.1}(Ni_{0.33}Co_{0.33})O_2$) is lower, but still significantly higher than that of $LiFePO_4$, which shows almost no energy release upon heating. This states the intrinsically safe character of phosphate-type olivines and the improbability to contribute to a thermal runaway. The reason is found in the strong P-O bond, low oxygen potential and thus high safety [14, 15].

But not only high temperatures are critical for lithium-ion batteries. At low temperatures the kinetics of $Li^+$-intercalation into graphite is slower. Instead of the intercalation process, the reduction of $Li^+$ to elemental Li may be favored, while recent studies found that this process takes place near the separator-graphite interface [17, 18]. The deposited Li can appear as a flat layer (plating) or in form of needle-shaped dendrites. The latter are critical since they can penetrate the separator and cause an internal short circuit [19–21].

Furthermore, electrolytes for lithium-ion batteries consist of a conducting salt (*e. g.* $LiPF_6$) in a carbonate-based solvent [22, 23]. These non-aqueous solvents provide a sufficient electrochemical stability window for high operating voltages, high conductivity and low viscosity. There exist several different carbonates and some typical compounds are ethylene carbonate (EC), propylene carbonate (PC) and dimethyl carbonate (DMC) which can be applied pure or as a mixture in order to attain specific characteristics [24, 25]. Despite their positive properties, carbonates involve a major problem due to their flammability and low flashpoint at approximately room temperature [26]. In case of overheating (*e. g.* as a consequence of a short circuit) it may ignite and even initiate a thermal runaway under unfavorable conditions [27].

The presented safety-critical processes in lithium-ion batteries are not only of theoretic nature, as incidents are regularly shifted into public awareness. Over the past few year some safety incidents related to lithium-ion batteries have even attracted global media attention. In 2013, an auxiliary power unit (APU) battery caught fire on board of a Boeing Dreamliner. The aircraft was grounded and empty of passengers, which prevented casualties and major damage [28]. Only nine days after this event a battery caught fire on an airborne Boeing Dreamliner enforcing an emergency landing [29]. These and further incidents increased the awareness of battery failure and the potential consequences. The result of this development were strict regulations on the transportation of lithium-ion batteries on passenger aircrafts [30]. In 2016, several exemplars of the Samsung Galaxy Note 7 exploded or caught fire only a few days after its market release. Property damages and fires in cars were reported in relation to these phone explosions [31]. The European and US aviation authorities EASA and FAA strongly advised not to use or charge the Samsung Galaxy Note 7 on board of aircrafts [32, 33]. Samsung stopped the production after a recall since replacement units caught fire as well [34, 35]. In the context of continuously increasing areas of application, these examples demonstrate the importance of highest safety standards in terms of production and operation of lithium-ion batteries. Resulting in grounded aircrafts and discontinued production, both examples state the economic impact of battery failure and the manufacturers' interest in reliable batteries. However, a desired high energy density and a maximum of safety are contradictory to a certain degree.

Nowadays, owners of houses with installed solar panels increasingly strive to improve their own domestic energy consumption rate. This can be realized by coupling solar panels and lithium-ion batteries [36]. The installed capacity depends on the specific circumstances but is usually in the range of several kWh [37]. The installation of large lithium-ion batteries in households requires highest safety standards due to the potential impacts of a battery failure. Current discussions range from missing uniform safety standards and norms to installation sites and emergency response tactics [38, 39]. Australian authorities even suggest allowing private energy storage systems only in separate fire bunkers [40]. High safety standards for home storage applications are also in the interest of reinsurers as building fires are associated with significantly higher losses in comparison to vehicle fires. All these various discourses confirm the safety awareness regarding lithium-ion batteries as home storage application.

As described above, the safety of a lithium-ion battery depends on several components such as electrolyte, cathode material or formation of lithium dendrites. But replacing the commonly used cathode material group of transition metal oxides by a safer material such as $LiFePO_4$ or $LiFeMnPO_4$ can contribute to a higher operational safety and reliability [41]. The suitability of $LiFePO_4$ for home storage and further applications has been approved and products are available on the market [42]. The following section will provide detailed information on the characteristics and applications of phosphate-based cathode active materials, describe their superior properties and discuss them in the context with commonly used layered oxides.

## 1.2. Properties and Applications of $LiFe_xMn_{1-x}PO_4$

The material $LiFe_xMn_{1-x}PO_4$ is an olivine-type phosphate compound, which is suitable as cathode active material in lithium-ion batteries. The Fe/Mn-ratio can vary in the range of $0 \leq x \leq 1$, whereby $LiFePO_4$ and $LiMnPO_4$ are obtained for $x = 1$ and $x = 0$, respectively. For all other values of x, $LiFe_xMn_{1-x}PO_4$ (abbreviated as $LiFeMnPO_4$ or LFMP) is obtained. Within the crystal structure Fe and Mn randomly occupy the same lattice position. Mn and Fe have the atomic numbers 25 and 26 and their cations $Mn^{2+}$ and $Fe^{2+}$ show very similar atomic radii ($r_{Mn^{2+}} = 0.83$ Å, $r_{Fe^{2+}} = 0.77$ Å). Thus, $Mn^{2+}$ and $Fe^{2+}$ readily substitute for each other since their difference in atomic radii is less than 15 % [43].

The fundamental suitability of $LiMPO_4$ ($M$= Fe, Mn, Ni or Co) was first demonstrated by Padhi et. al. back in 1997 [44]. It provides high stability during lithium extraction and insertion and in theory a specific capacity of approximately 170 mAh·g$^{-1}$ (the specific capacity comprises the molar mass and varies slightly depending on the metal ratio in $LiMPO_4$). A problem of $LiNiPO_4$, $LiCoPO_4$ or mixed as $LiNi_xCo_{1-x}PO_4$ is the high operating voltage of $Ni^{2+}/Ni^{3+}$ (5.1 V vs. $Li/Li^+$) and $Co^{2+}/Co^{3+}$ (4.8 V vs. $Li/Li^+$) [45, 46]. Such high operating voltages are beyond the electrochemical window of ≈ 4.5 V vs. $Li/Li^+$ for commonly used electrolytes. Although sulfone-based electrolytes with electrochemical stability up to 5.5 V have been investigated and also tested in combination with $LiNiPO_4$, the practical use of Ni- and Co-based phosphor-olivines is still bound to the development of new electrolytes [47–49]. In contrast, the operating voltages of $Fe^{2+}/Fe^{3+}$ (3.5 V vs. $Li/Li^{+}$) and $Mn^{2+}/Mn^{3+}$ (4.1 V vs. $Li/Li^{+}$) are within the electrochemical window, which allows the use in combination with available electrolytes [50]. For this reason current research and development aims towards Mn-rich $LiFe_xMn_{1-x}PO_4$ [51].

The crystal structure of $LiFe_xMn_{1-x}PO_4$ is illustrated in Figure 2. Oxygen atoms (red) are arranged in a nearly hexagonal close packing (hcp). In the hcp arrangement $2n$ tetrahedral sites are formed for $n$ atoms resulting in 8 tetrahedral sites per 4 oxygen atoms. Phosphorus (purple) occupies thus ⅛ of the available tetrahedral sites. The phosphorus atoms are covalently bonded to 4 oxygen atoms forming a tetrahedral arrangement. In the hcp structure also $n$ packing atoms form $n$ empty octahedral sites. From the four oxygen atoms of the net formula therefore result four octahedral sites. The octahedral sites are only ½ occupied in total by an ordered arrangement of either Li (green) or Fe/Mn (white) atoms. The Li coordination polyhedra (green polyhedra in Figure 2) are linked by edges and form $Li^{+}$ diffusion channels. These diffusion channels occur only along one structural axis resulting in a one dimensional $Li^{+}$ (de-) intercalation [44, 52]. In comparison, the structure of layered oxides allows a two dimensional $Li^{+}$ (de-) intercalation [53].

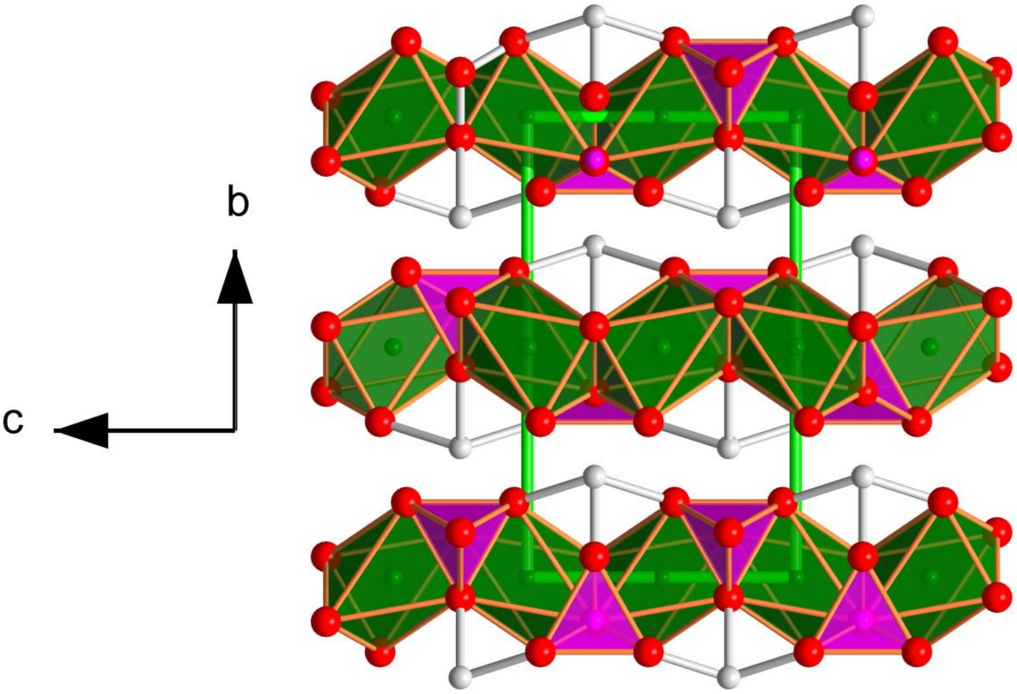

Figure 2: Crystal structure of $LiFe_xMn_{1-x}PO_4$ (space group: $Pnma$) projected along the $a$-axis. The unit cell is defined by the light green frame. $Li^{+}$ atoms are located within green coordination polyhedra, P atoms are located within purple tetrahedrons. Fe and Mn are white colored and cannot be distinguished since the actual distribution is randomly (coordination polyhedra are not marked). $Li^{+}$ diffusion is only possible via connected Li coordination polyhedra along the $c$-axis. Image created with the Endeavour software.

The ordered olivine structure of $LiFe_xMn_{1-x}PO_4$ has semiconductor-like properties with a very low electronic conductivity of approximately $\approx 10^{-9}\,S\,cm^{-1}$, which is a substantial obstacle for any battery application [54]. In order to overcome this problem, the particle size was subsequently reduced to the nano-scale and also different synthesis techniques and doping with other metals were studied to improve the electrochemical characteristics. Nano-sized particles provide large specific surfaces of several $m^2\,g^{-1}$ which lead to minimized diffusion pathways. Another effective method to improve the electrochemical capability and kinetics is carbon coating of $LiFe_xMn_{1-x}PO_4$ particles, resulting in good fast-charging properties [55–60].

Regarding the characteristic charge curves as illustrated in Figure 3, LFP and LFMP provide flat redox plateaus over a wide range of State of Charge (SOC). At SOC = 0 % (beginning of charge) LFP/LFMP are completely lithiated. At SOC = 100 % (end of charge) the material is completely de-lithiated. Upon de-lithiation of $LiFePO_4$ and $LiFe_xMn_{1-x}PO_4$ a phase transition to thermodynamically stable $FePO_4$ and $Fe_xMn_{1-x}PO_4$ occurs, respectively.

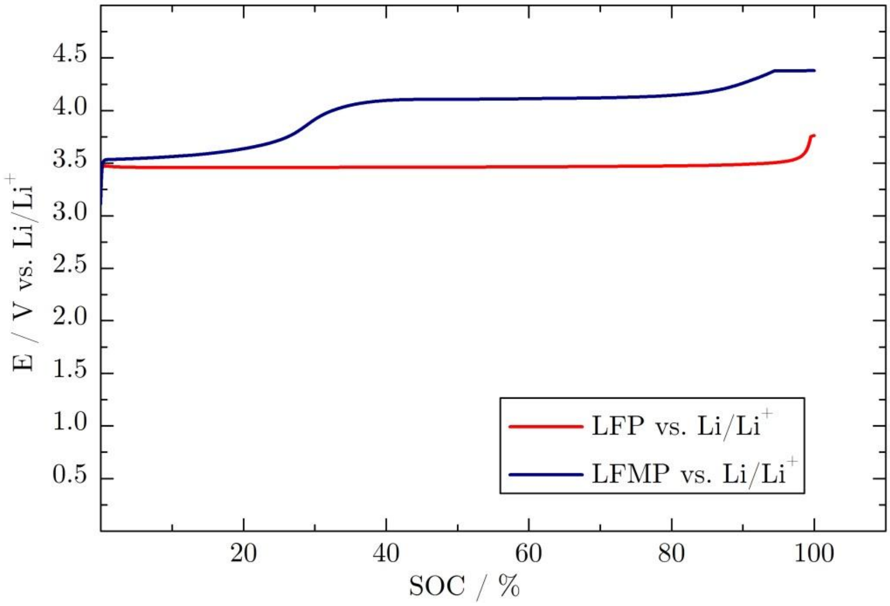

Figure 3: Comparison of redox plateaus of $LiFePO_4$ vs. $Li/Li^+$ and $LiFe_{0.33}Mn_{0.67}PO4$ vs. $Li/Li^+$ during the charge process of cells using graphite as anode active material. Voltage curves are obtained from a 3-electrode-setup (Swagelok®-cell).

For LFMP two redox plateaus can be observed. The first one at approximately 3.5 V vs. $Li/Li^+$ corresponds with the $Fe^{2+}/Fe^{3+}$ redox plateau. This plateau is followed by the $Mn^{2+}/Mn^{3+}$ redox plateau at approximately 4.1 V vs. $Li/Li^+$. The length of the

$Fe^{2+}/Fe^{3+}$ and $Mn^{2+}/Mn^{3+}$ is directly correlated to the Fe/Mn ratio in $LiFe_xMn_{1-x}PO_4$ indicating that $LiFe_xMn_{1-x}PO_4$ shown in Figure 3 is a Mn-rich $LiFe_{0.33}Mn_{0.67}PO_4$.

The higher voltage of the $Mn^{2+}/Mn^{3+}$ redox plateau and the higher resulting energy density explains the advantage of (partial) substitution of Fe by Mn. The higher voltage of $Mn^{2+}/Mn^{3+}$ also suggests the complete substitution of Fe, but it is difficult to obtain electrochemically active $LiMnPO_4$ and observable (dis-)charge characteristics are disadvantageous [61–63]. Furthermore, the intrinsically safe character of $LiFe_xMn_{1-x}PO_4$ does not fully apply to (partially de-lithiated) $LiMnPO_4$ since it is not thermodynamically stable. In the de-lithiated form $MnPO_4$ releases oxygen above 150 °C and considerable heat generation (884 $J \cdot g^{-1}$) upon reaction with the electrolyte occurs [64].

The fact that $LiFe_xMn_{1-x}PO_4$ (with the exception of $LiMnPO_4$) is a material with two thermodynamically stable boundary phases is a substantial distinguishing feature in relation to commonly used layered oxide-type cathode active materials such as $LiNi_xMn_yCo_{1-x-y}O_2$, which shows a solid-solution behavior. Layered oxides thus do not undergo a phase transition during the normal (dis-)charge process. In the (partially) de-lithiated state, layered oxides are thermodynamically unstable and tend to decomposition and oxygen release under heat exposure. Despite its thermodynamic instability during de-lithiation the host structure is maintained due to kinetic reasons. This allows the use of layered oxides as cathode active material [65–70].

In contrast, the stability of $LiFe_xMn_{1-x}PO_4$ can be explained by the strong covalent P-O bond preventing the release of oxygen up to high temperatures. In the case of battery failure and heat development, the electrolyte will decompose and react with different constituents of the battery. On the anode side the SEI layer and the graphite itself will decompose at temperatures of about 80 – 120 °C and above 250 °C, respectively [71, 72]. Concerning cathode materials, different onset temperatures can be found (assuming SOC = 100 %). Layered oxides, such as $LiNi_xCo_yAl_zO_2$ (NCA), $LiCoO_2$ (LCO) and $LiNi_xMn_yCo_zO_2$ (NMC) begin to decompose at temperatures of 170, 200 and 260 °C and enthalpies of 941, 407 and 910 $J g^{-1}$, are found respectively [53, 73, 74]. The overall enthalpy can vary and increases with the degree of de-lithiation and relative Ni content [75]. In contrast the decomposition of $LiFePO_4$ has an onset temperature of 310 °C and an enthalpy of only 145 $J g^{-1}$ according to [76, 77]. Other studies found an onset temperature of 245 °C and enthalpies in the range of 147 to 250 $J g^{-1}$ [78, 79]. Generally, the values state that $LiFePO_4$ shows better thermal stability and significantly lower enthalpy in comparison to layered oxides.

Other advantages besides the thermal stability of $LiFe_xMn_{1-x}PO_4$ arise from the elemental composition due to its environmental friendliness, low toxicity, costs and availability [80, 81]. In 2017, the global reserves of iron and manganese were $8.2 \cdot 10^{10}$ and $6.9 \cdot 10^{8}$ tons, respectively [82, 83]. Both materials are available on a sufficient scale for industrial needs. In contrast, todays layered oxides generally contain cobalt and its worldwide reserves are estimated to be as low as $7 \cdot 10^{6}$ tons. The current high demand for lithium-ion batteries already results in an upcoming cobalt shortage and rising prices [84].

The current availability of $LiFe_xMn_{1-x}PO_4$-based products is mainly limited to Mn-free $LiFePO_4$. For mobile applications such as electronic devices and electric vehicles oxide layered cathodes are still the material of choice due to the higher specific and volumetric capacity [85]. Commercial $LiNi_{0.8}Co_{0.15}Al_{0.05}O_2$/graphite cells provide capacities of up to 200 $mAh\,g^{-1}$, 3.7 V average operating voltage and a volumetric capacity of 700 $mAh\,cm^{-3}$ compared to 165 $mAh\,g^{-1}$, 3.4 V average operating voltage and 589 $mAh\,cm^{-3}$ for $LiFePO_4$ [86]. So far, existing mobile applications of $LiFePO_4$ are limited to niche products like pedelecs, scooters or starter batteries, but small-series electric vehicles were also equipped with $LiFePO_4$-based cathodes [87–90]. In the marine sector $LiFePO_4$ batteries are regarded as a suitable replacement for lead-acid batteries [91]. The benefits of $LiFePO_4$ come to bear in environments where energy density and weight is of minor importance but operational safety and reliability needs to be at highest standards. Both criteria are met for stationary and household applications. Different studies have discussed and considered $LiFePO_4$ as the optimum cathode material for solar energy storage or off-grid solutions for remote places and commercial solutions are available on the market [42, 92–98]. In contrast, Mn-containing $LiFe_xMn_{1-x}PO_4$, especially $LiMnPO_4$, is still regarded to be in the research stage, but first products are introduced to the market [86, 99]. The commercialization of $LiFe_xMn_{1-x}PO_4$ is hindered by some unsolved obstacles in terms of aging and operational deficits. An overview of issues related to aging is given in the following chapter.

## 1.3. Aging mechanisms related to $LiFe_xMn_{1-x}PO_4$

Over the past years, several studies focused on the aging of $LiFePO_4$ and investigated the influence of various storage conditions like moist environments, hot air or the immersion into water and the effects on the electrochemical properties. Moist atmosphere is supposed to initiate a partial phase transition from $LiFePO_4$ to $LiFePO_4(OH)$ under oxidation of $Fe^{2+}$ to $Fe^{3+}$, whereas a formula for the intermediate material was proposed as $Li_xFePO_4(OH)_x$. The phase transition was found to be reversible and the initial capacity and performance can be attained by a thermal treatment under inert atmosphere [100]. Warm and moist atmosphere also causes the reversible formation of $FePO_4$ and $Li_3PO_4$ [101]. Exposure to air at ambient temperature leads to spontaneous $Li^+$ de-intercalation and increased impedance. But this effect disappears after the first cycle [102]. In contrast, under hot air ($T \leq 200$ °C) the formation of a $Fe_2O_3$ side phase and highly defective $LiFePO_4$ unit cell can be observed [103]. The immersion of $LiFePO_4$ into water has been described to be responsible for a partial loss of carbon coating. Water subsequently attacks the surface of $LiFePO_4$ particles and lithium and phosphate species can be detected in the water. The carbon coating is assumed to protect the $LiFePO_4$ particles for a certain period of time, but the protective effect is more efficient for moist atmosphere instead of direct immersion into water. The stability of the carbon coating also depends on the synthesis and it is more protective when obtained from a solid state reaction synthesis instead of a hydrothermal procedure [104]. Contact to water also induces the formation of a $Li_3PO_4$ layer on the particle surface. But no significant influence of this layer on the battery performance is found [105]. A moisture contamination of the electrolyte is associated with the generation of HF. The formed HF effects the dissolution of Fe from $LiFePO_4$, and hence a decreased cell performance and elevated capacity loss. This degradation can be effectively suppressed by carbon coating as it prevents surface corrosion of $LiFePO_4$ particles [106]. In general, $LiFePO_4$ is stable in electrolytes containing $LiPF_6$ and only very low Fe-dissolution rates are observable. But at higher temperatures (60 °C) the Fe-dissolution rate raises significantly and developing resistive layers on the particle surface cause capacity fading and poor kinetics [107].

Another aging mechanism which causes accelerated capacity fading is the dissolution of Mn-ions from the $LiFe_xMn_{1-x}PO_4$ host structure. This effect is not only characteristic for $LiFe_xMn_{1-x}PO_4$ and has also been described for Mn-containing layered oxides and spinels [108, 109]. The reasons for capacity loss upon Mn-dissolution include different aspects. For reasons of charge balancing, each dissolved

$Mn^{2+}$ or $Mn^{3+}$-ion prevents the de-intercalation or re-intercalation of active $Li^{+}$-ions from or into the $LiFe_xMn_{1-x}PO_4$ host structure. But the observable Mn-dissolution rates are in the range of several ppm and thus are not directly responsible for considerable capacity loss. The reasons for capacity loss are rather caused by the migration of Mn-ions to the anodic graphite surface. According to previous research, Mn-ions are incorporated into the SEI-layer located on the anode surface causing an increased growth due to maintained conductivity along the SEI-layer and ongoing electrolyte reduction [110]. A schematic illustration of a Mn-free and Mn-contaminated SEI-layer is given in Figure 4. The SEI-layer is formed under consumption of active lithium and thus, increased SEI growth leads to additional capacity loss. It is known that Mn and Fe dissolve in the same ratio as they are present in $LiFe_xMn_{1-x}PO_4$ [111].

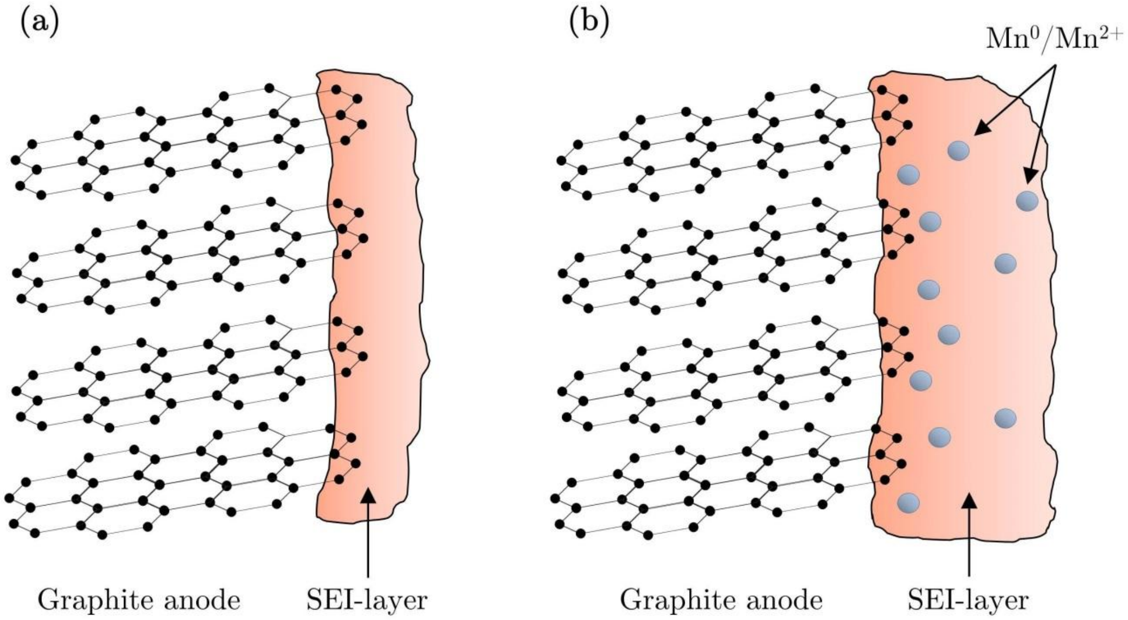

Figure 4: Schematic drawing of SEI layers on the graphite anode: (a) SEI-layer built up in a cell with Mn-free cathode material; (b) Increased SEI-layer growth as a result of incorporated Mn.

As well as in olivine-type $LiFe_xMn_{1-x}PO_4$ transition metal dissolution in layered oxides is not limited to Mn as elements like Ni and Co are also deposited on the anodic SEI-layer [112, 113]. It is known that metal ions can be deposited in different regions of the SEI-layer and different oxidation states are found depending on an insertion in the inner or outer region of the SEI-layer [108, 114]. Transition metal ions like $Ni^{2+}$ and $Co^{2+}$ are supposed to be deposited in the outer layer of the SEI and are not reduced, while $Mn^{2+}$ can be found in the inner regions close to the interface of graphite and SEI. The close proximity to the actual graphite surface allows the reduction to $Mn^0$ and in the presence of electrolyte a $Mn^{2+}/Mn^0$ catalyzed redox couple causes ongoing electrolyte reduction, loss of active lithium and capacity [115]. This aging mechanism emphasizes the special role of Mn-dissolution also attributed to $LiFe_xMn_{1-x}PO_4$. Overall, the Mn-dissolution rates observable for $LiFe_xMn_{1-x}PO_4$ do not seem to exceed those ones of layered oxides [116].

## 1.4. Neutrons vs. X-rays

Through the discovery of X-rays by Wilhelm Conrad Röntgen in 1895, the basis for a completely new field of structural and radiographic research had been created [117, 118]. In the 1950s, Bertram Brockhouse and Clifford Shull worked on spectroscopy and diffraction methods based on uncharged particles. Both were honored with the Nobel Prize in 1994 for their substantial contribution to the development and establishment of neutron diffraction techniques, providing further scientific opportunities [119–122]. In the upcoming years, neutron research facilities were established in Germany, France, USA and other countries [123–125]. The interest in neutrons was motivated by their different properties compared to X-rays.

Both X-rays and neutrons have wave- and particle-like character. This means that they have a mass but simultaneously show wave properties like constructive and destructive interference [126]. X-rays interact with the electron shell of an atom. Since the number of electrons is directly correlated with the atomic number, a constantly increasing cross-section of X-rays can be observed with increasing atomic number. As the number of electrons remains constant for isotopes of an element, a differentiation of those is not possible [127]. In contrast, neutrons do not interact with the electron shell, but with the atomic nucleus. There is no systematic trend in cross-section and atomic number, which means that the cross section varies randomly with increasing atomic number. As isotopes mean a different composition of the atomic nucleus, the cross section of neutrons can vary considerably and enables the distinction on an isotope level [128–130]. Neutrons can also allow the disambiguation of neighboring elements and the scattering power of very light elements, like Li, is in the same scale as that of heavier elements.

As illustrated in Figure 5 for selected elements, cross sections of X-rays increase constantly with increasing atomic number. In contrast, neutrons do not show a direct correlation between cross section and atomic number as it varies randomly. Figure 5 also illustrates that X-rays have only positive scattering lengths, which increase with the atomic number, while neutrons can have a positive or negative scattering length. Again, the reason for this difference is found in the fact that X-rays are scattered at the electron shell, while neutrons interact with the atomic nucleus. The interaction with electron shell or atomic nucleus also results in a stronger or lighter decrease of Bragg peak intensities with increasing $2\theta$-angles [131, 132].

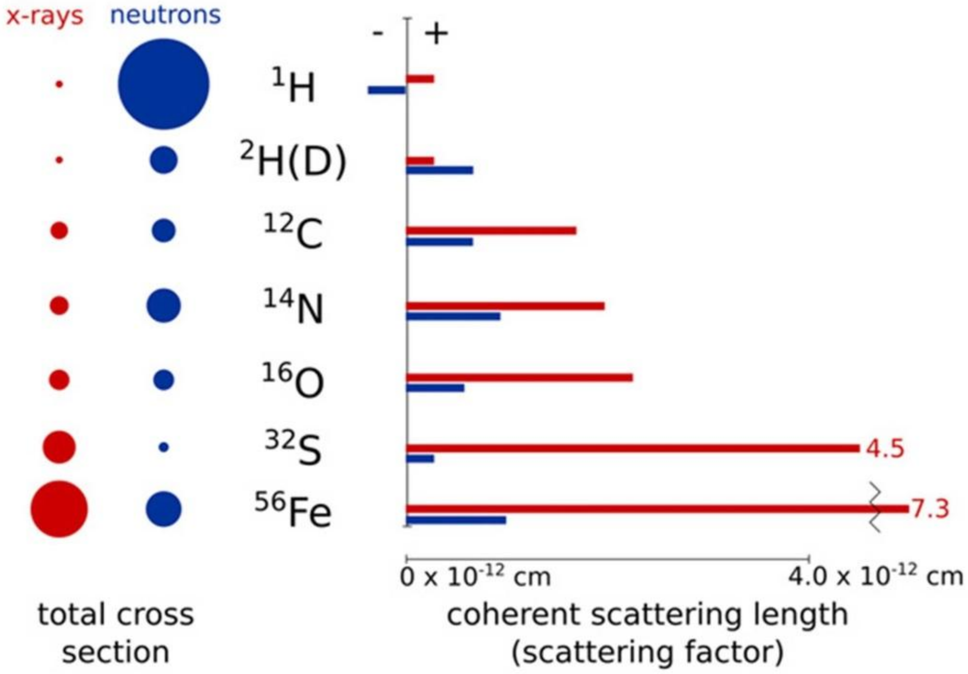

Figure 5: Comparison of cross sections of selected elements for X-rays and neutrons. Image from [133] based on data from [134–136].

The different cross sections shown in Figure 5 also explain the supplementary character of X-rays and neutrons. As the lightest element, hydrogen ($^{1}$H) is almost invisible for X-rays, while it has a very high cross section for neutrons. On the contrary, sulfur ($^{32}$S) has a low cross section for neutrons, but – in terms of detectability - sufficient cross section for X-rays. From the scientific perspective, the different nature of X-rays and neutrons and their interaction with matter is of importance since the complementary character of both provides suitability for a wide range of research issues.

## 1.5. Neutrons in lithium-ion battery research

Due to their special properties as described in *1.4 Neutrons vs. X-rays,* neutron-based analytical methods have become a versatile and established resource to investigate scientific issues in the context of lithium-ion batteries.

This chapter introduces some neutron-based methods applied to lithium-ion batteries and outlines related research issues and results.

Neutron diffraction (ND) basically follows the same principles as X-ray diffraction and can be described by the Bragg-Equation:

$$n\lambda = 2d\sin(\theta) \tag{3}$$

In equation (3), $n$ is an integer multiple of the wavelength $\lambda$, $d$ the interplanar distance between two lattice planes and $\theta$ the scattering angle between incident beam and the lattice plane [137].

ND is suitable to investigate different phenomena related to lithium-ion batteries, such as lithium (de-)intercalation into anodic graphite, which is the most commonly used active material for anodes in lithium-ion batteries [138–140]. *In-situ* ND has been applied to study the kinetics of lithium (de-)intercalation at different C-rates and temperatures and it was found that inhomogeneous distribution of lithium in graphite and the time of cell relaxation is elevated at low temperatures and higher (dis-)charge currents [141]. *In-situ* ND also helped to understand the correlation between voltage relaxation, temperature and lithium deposition on the graphite surface (lithium plating). Plating instead of intercalation into graphite increases at low temperatures and correlates with the charge current [142]. In case of a commercial NMC/graphite cell, lithium plating can reach values of 19 % of the nominal capacity if it is charged at a C/5 rate and a temperature of -20 °C [143]. Understanding the mechanisms of lithium plating is important since it can come along with lithium dendrite formation and possible occurrence of an internal short circuit and thermal runaway [19, 144–147].

In the field of cathode materials, ND was applied to study the $Li^+/Ni^{2+}$ disorder in the lattice of the layered oxide NMC with the result that $Li^+/Ni^{2+}$ site exchange negatively affects the diffusion kinetics due to a higher $Li^+$ migration barrier [148]. But also Ni/Mn disorders upon different synthesis methods and their influence on the electrochemical performance were investigated on the spinel type $LiMn_{1.5}Ni_{0.5}O_4$

structure. A variation in synthesis temperature profiles causes significantly different crystal structures with Ni/Mn ordered or disordered variants [149]. On the other hand, ND studies on commercial LFP/graphite cells (18650) helped to distinguish reasons and to exclude potential LFP degradation mechanisms responsible for capacity fading upon long-term cycling [150].

Neutron imaging (NI) or neutron radiography (NR) is a non-destructive method, which has been developed since as early as 1935 [151]. As a versatile technique in materials science it has also been applied to study various aspects in the field of lithium-ion batteries. When a neutron beam passes through a sample, it will be attenuated depending on the element and its thickness at a specific location of the sample [152]. The principles of neutron imaging can be described by the Law of Lambert-Beer as shown in equation (4). The transmission $T$ is defined by the ratio of the intensity after passing through the sample ($I$) and the incident beam $I_0$. The specific attenuation coefficient of the irradiated object is described by $\mu$ and its thickness by $d$:

$$T = \frac{I}{I_0} = e^{-\mu \cdot d} \tag{4}$$

After passing through the sample, the neutron beam shows a locally different distribution of intensity. Since neutrons are electrically neutral, detectors for image generation rely on second order effects. This means that in the detector neutrons are captured by highly absorbing materials such as $^{6}$Li, $^{10}$B and $^{155}$Gd, which emit a secondary radiation (*e. g.* γ-radiation) capable to excite a scintillator screen. The emitted light upon de-excitation can then be recorded by a CCD-camera (CCD = Charge-Coupled Device) [153–155]. The application of CCD-cameras has mainly replaced the former method using X-ray-sensitive films [151, 156].

The manufacturing process of a lithium-ion battery includes the step of electrolyte filling. The subsequent wetting, which means the homogenous distribution of the electrolyte inside the battery, is decisive for the quality. Since wetting is a time-consuming and limiting factor in the manufacturing process, it is of high interest to minimize the time of this step without negative influence of the battery performance [157, 158]. Knoche *et. al.* applied NI in order to visualize the electrolyte filling process of a lithium-ion battery and derived optimized manufacturing processes and potential faults [159].

Gas evolution in lithium-ion batteries is a well-known problem associated with capacity fading and decreasing performance [160, 161]. It occurs as a concomitant reduction of electrolyte during the formation of the anodic SEI-layer but also as a

consequence of residual traces of water within the battery [162–164]. The gas evolution in batteries with different combinations of anode and cathode active materials has been studied by means of neutron imaging. It was found that the volume of evolved gas depends significantly on the active material and implies also the correlation of gas evolution and transmission metal dissolution [165, 166]. Not only the electrode active material influences the gas evolution, but also the composition of the electrolyte can considerably affect gassing [167].
NI was also used to investigate the diffusion behavior of lithium-ions in the anode active material $Li_4Ti_5O_{12}$ (LTO) [168, 169].

Another method, which involves neutrons indirectly, is Positron Annihilation Spectroscopy (PAS). Positrons are positively charged counterparts of electrons [170]. A possibility to generate positrons is the capture of thermal neutrons in Cadmium and subsequent positron-electron pair production from absorption of high energetic prompt $\gamma$-rays [171, 172]. One application of PAS in the field of lithium-ion batteries is the investigation of structural defects. PAS has been successfully applied to describe the evolution of irreversible defects in the cathode active material NMC occurring upon (de-)lithiation. During irradiation, positrons are diffusing through the NMC-lattice. The positrons can either annihilate with an electron, resulting in the emission of 2 $\gamma$-quanta, or be trapped in a metal atom vacancy in the lattice prior to annihilation. Thus, the lifetime of a positron is directly related to the concentration of vacancy-type defects in the NMC-lattice, which can be determined via PAS [173]. Positrons have also been applied to investigate defect formation in other cathode materials like LCO and LFP [174, 175].

## 1.6. Neutron source and instruments at FRM II

This chapter briefly introduces the neutron source of the Forschungsreaktor München II (FRM II) at the Heinz Maier-Leibnitz Zentrum (MLZ) in Garching/ Germany and the instruments which were used to carry out neutron experiments.

The cylindrically shaped fuel element of the neutron source has a height of 70 cm, a diameter of about 24 cm and consists of a uranium-silicon compound and aluminum. The inner part of the cylinder contains 113 involute curved fuel plates. Once the radioactive decay of the fuel element is initiated at one of its sides, it reacts for approximately 60 days while the reactive zone is constantly positioned on the height of the beam tubes by gradual movement of the fuel element. The neutron flux depends on the distance from the fuel element. Using $D_2O$ instead of $H_2O$ as a moderator around the fuel element shifts the maximum neutron flux approximately 12 cm outside the fuel element wall. At this position He-filled beam tubes efficiently guide the neutrons out of the reactor pool. During operation, the fuel element provides a continuous neutron flux of $8 \cdot 10^{14}\,\mathrm{n} \cdot \mathrm{cm}^{-2}\mathrm{s}^{-1}$ at a thermal output of 20 MW. Depending on the scientific scope, the energy of produced neutrons can be adapted in a wide range of approximately $10^{-6}$ eV (ultra-cold neutrons) to 2 MeV (fission neutrons). [176–183]

Neutron diffraction experiments were carried out at the high-resolution powder diffractometer SPODI, which is schematically shown in Figure 6. The diffractometer uses thermal neutrons and is operated with a focus on complex structural characterization of materials such as minerals, alloys, superconductors and materials for lithium-ion batteries [184].

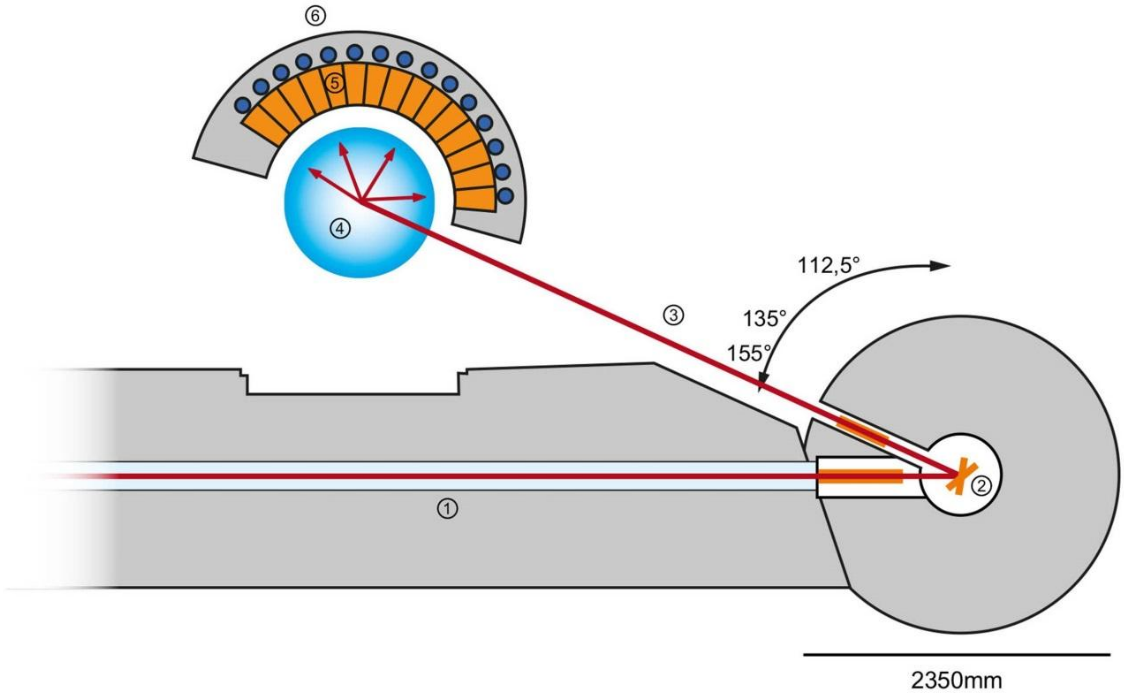

Figure 6: Schematic illustration of the instrument SPODI: 1: Neutron guide, 2: Monochromator, 3: Optimal collimation, 4: Sample table, 5: Collimator array, 6: Detector array; modified image from [184].

The instrument is characterized by a high take-off angle of 155° and a detector array consisting of 80 position-sensitive $^3$He-tubes. Each detector covers an angle of 2°. This results in an angular range of 160° for the detector array. During recording of diffraction patterns, the detector array is moved stepwise, whereby the typical step width is 0.05° (repeated 40 times resulting in a total shift of 2°) [185, 186].

Neutron imaging experiments were carried out at ANTARES, which is connected to the neutron beam port SR-4a. A schematic drawing of ANTARES is shown in Figure 7. The instrument allows standard two-dimensional radiographic imaging as well as three-dimensional computer tomography by step-wise rotation of the sample. Special setups such as stroboscopic and polarized neutron imaging extend the instrumental possibilities.

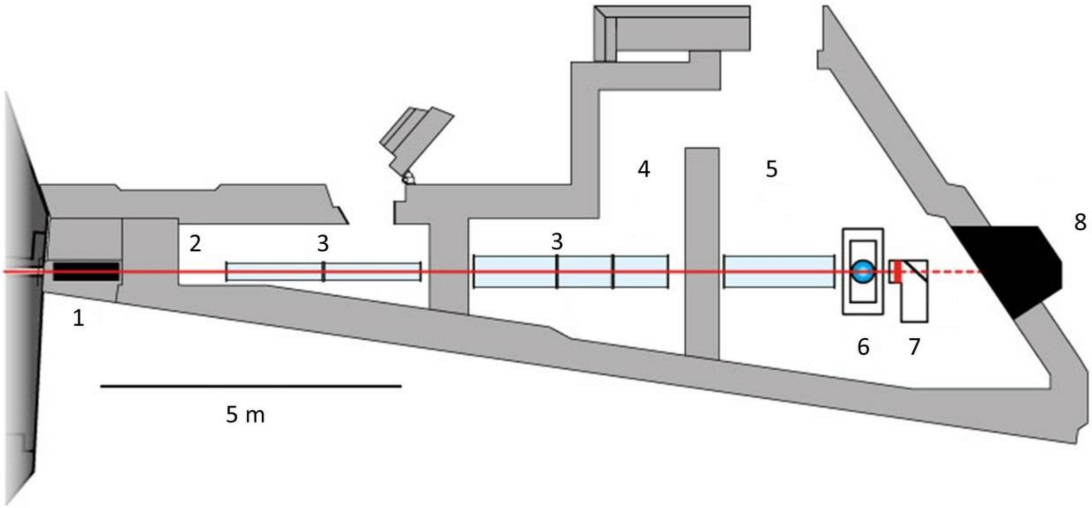

Figure 7: Schematic drawing of the instrument ANTARES: 1: Beam shutter, 2: Chamber 1, 3: Flight tubes, 4: Chamber 2, 5: Chamber 3, 6: Sample space, 7: Detector, 8: Beam stop; modified image from [187].

Typical applications range from geological to engineering issues and fundamental research on ferromagnetic phase transitions.

The instrument uses cold neutrons and a double crystal monochromator allowing the wavelength to be set to 1.4 Å - 6.0 Å. The neutron flux depends on the collimation and ranges from $2.6 \cdot 10^5$ $n \cdot cm^{-2}s^{-1}$ to $4 \cdot 10^8$ $n \cdot cm^{-2}s^{-1}$. The maximum beam size is 35 x 35 cm [176, 187–189].

Prompt Gamma Activation Analysis measurements were performed at the instrument named PGAA. It uses cold neutrons from the neutron beam tube NL4b with an average energy of 1.83 meV and wavelength of 6.7 Å. The basic experimental setup is illustrated in Figure 8.

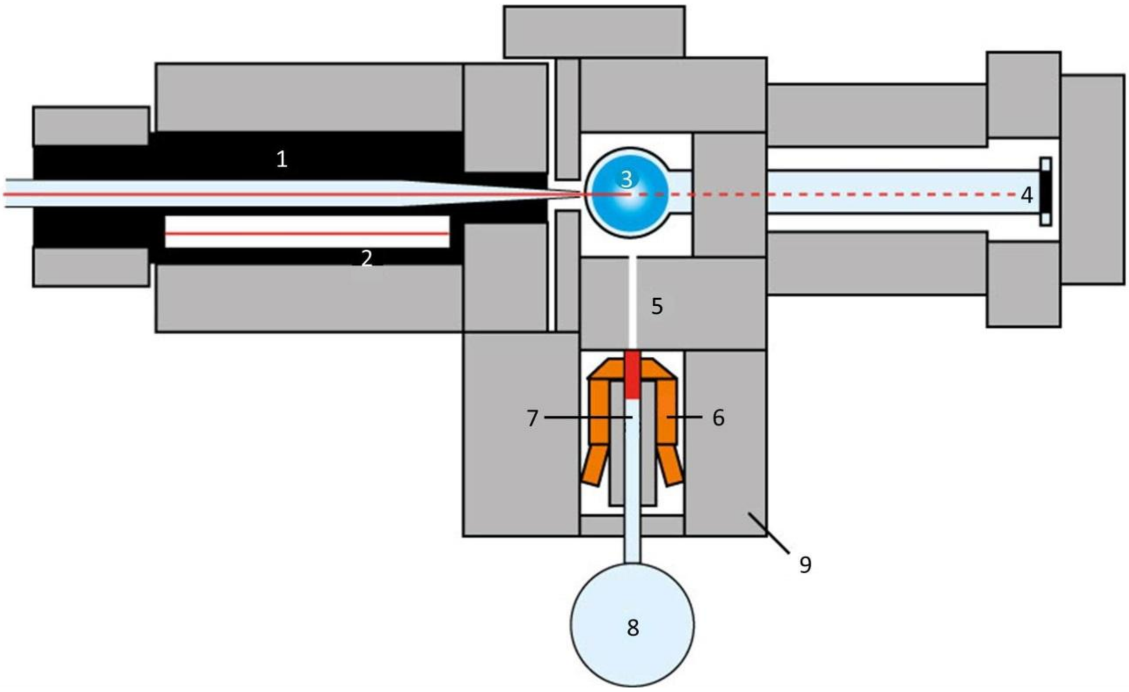

Figure 8: Drawing of the instrument PGAA: 1: Elliptical neutron guide, 2: Neutron collimator, 3: Sample chamber, 4: Beam stop, 5: Gamma collimator, 6: BGO scintillator, HPGe detector, 8: Dewar, 9: Shielding; image modified from [190].

PGAA allows the non-destructive measurements of gaseous, liquid and solid samples. Applications of PGAA range from archaeology and environmental sciences to geology and new materials. The instrument can be modified in order to conduct Neutron Depth Profiling (NDP) measurements [190]. Its suitability for measurements on components of lithium-ion batteries has been shown recently [113].

# 2. Experimental methods

This section provides some background information on experimental setups and methods with a focus on full-cell preparation and testing as well as experimental setups for neutron experiments.

All electrode slurries were prepared by using a dissolver as shown in Figure 9. At high numbers of rotation the dissolver disc provides a sufficient energy for homogeneous distribution of all constituents and a smooth slurry appearance. Many parameters such as number of rotation, volume of the dissolver vessel, diameter and immersion depth of the dissolver disc and viscosity influence the process and quality of the obtained slurry.

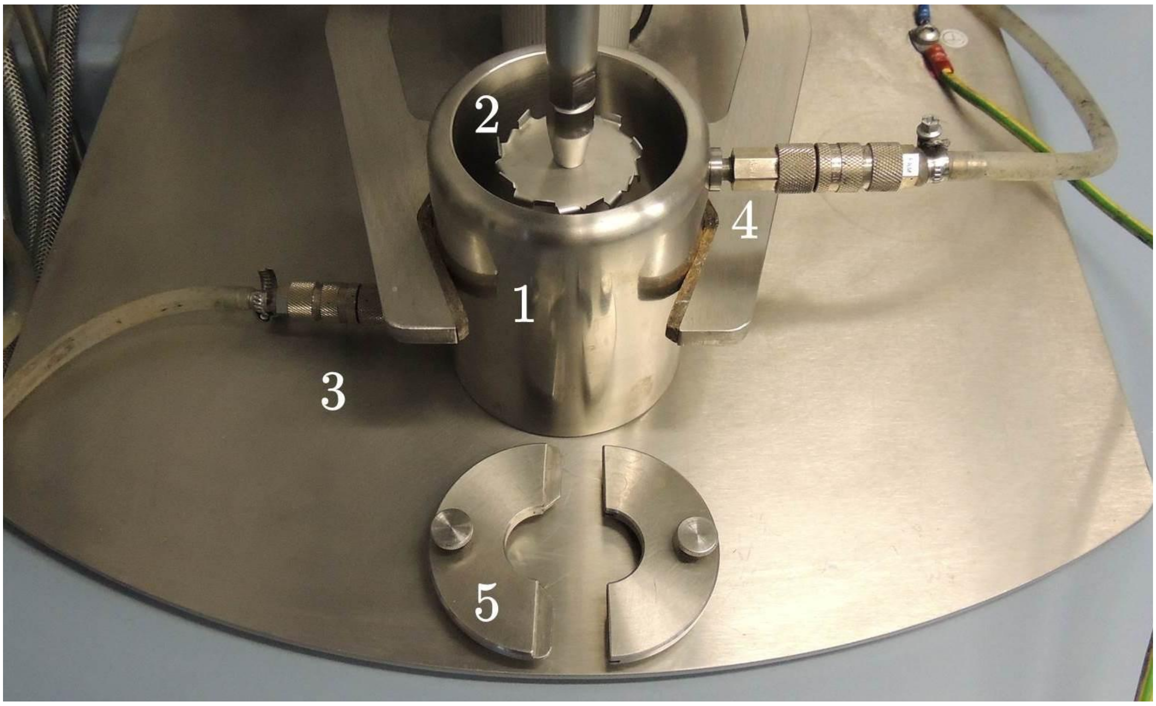

Figure 9: Image of the dissolver for slurry preparation: 1: Double-walled dissolver vessel, 2: Dissolver blade, 3: Cooling water inlet, 4: Cooling water outlet, 5: Cover for dissolver vessel.

Parameters like container volume, filling level, dissolver disc diameter and distance from bottom should be adjusted in such a way that the so-called doughnut-effect occurs. This means that the shaft and dissolver disc are partially visible and a laminar rolling flow pattern is achieved [191]. During dispersion the slurry can heat up due to energy intake resulting in a potential loss of solvent. For this reason the dissolver vessel is double-walled and allows the supply of cooling water. The dissolver vessel can be covered in order to minimize the entry of foreign particles.

The prepared slurries were processed to electrodes by using a roll-to-roll coater as illustrated in Figure 10a. The dimensions of the coater are equally suitable for short and long coating lengths. The coater can handle and roll up electrode rolls of several hundred meters. But likewise about only 2 m of unused electrode foil are necessary to prepare the roll-to-roll process, which means a relatively low waste of material for small electrode batches. The coater can be operated with a permanently installed doctor blade with continuously adjustable gap. But it is also possible to work with a standard doctor blade with invariable gap positioned in front of a transversely fixed metal stick as depicted in Figure 10b. This is a simple and well-functioning solution, but continuous slurry feed should be noted in avoidance of a varying coating thickness.

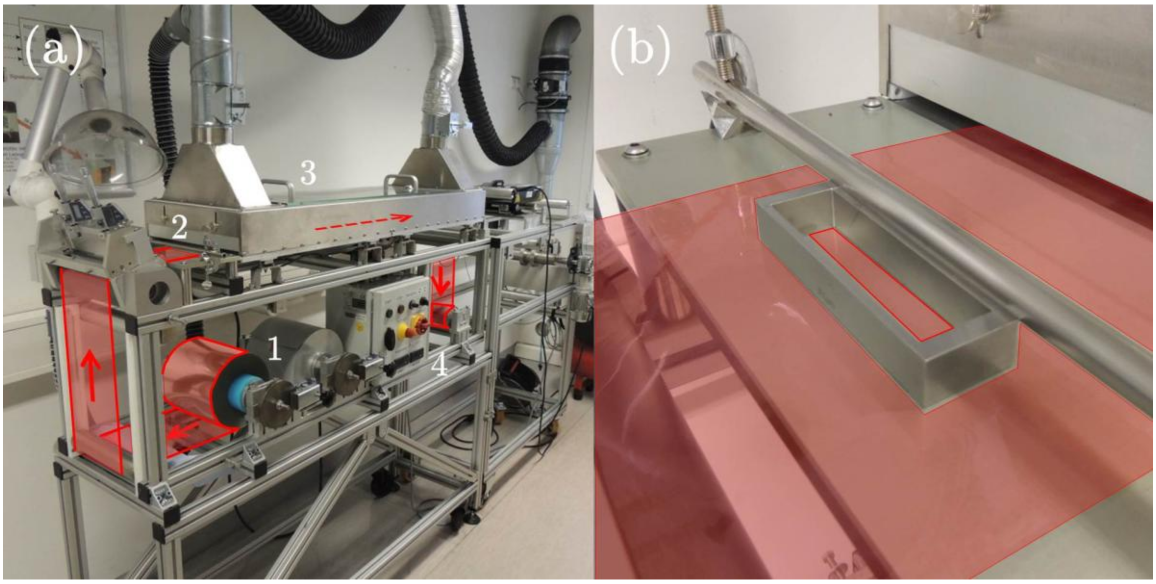

Figure 10: Image of the electrode coater. Guidance and direction of the electrode foil is schematically illustrated in red. (a) 1: uncoated and rolled up electrode foil, 2: position of doctor blade, 3: drying line with exhaust extraction, 4: coated and rolled up electrode foil; (b) Detail of doctor blade on top on an electrode foil. The metal stick keeps the doctor blade in position.

The wet electrode passes a cased drying line with two individual heating zones. Evaporating solvents are directly drawn off by the connected ventilation system. The feed rate of the electrode foil can be adjusted to the solvent and coating thickness of the slurry.

Subsequently, the prepared electrodes in combination with a separator are laminated by using a roll laminator as shown in Figure 11. The lamination step allows a tight connection of the cathode, separator and anode. The laminator has three individual heating zones and provides the option of pressure and gap adjustment. For a successful lamination it is important that the separator can be laminated. This can be achieved by a special activation (*e. g.* deposition of PVDF-fibers by electro spinning) or choosing a separator made of lamination capable material.

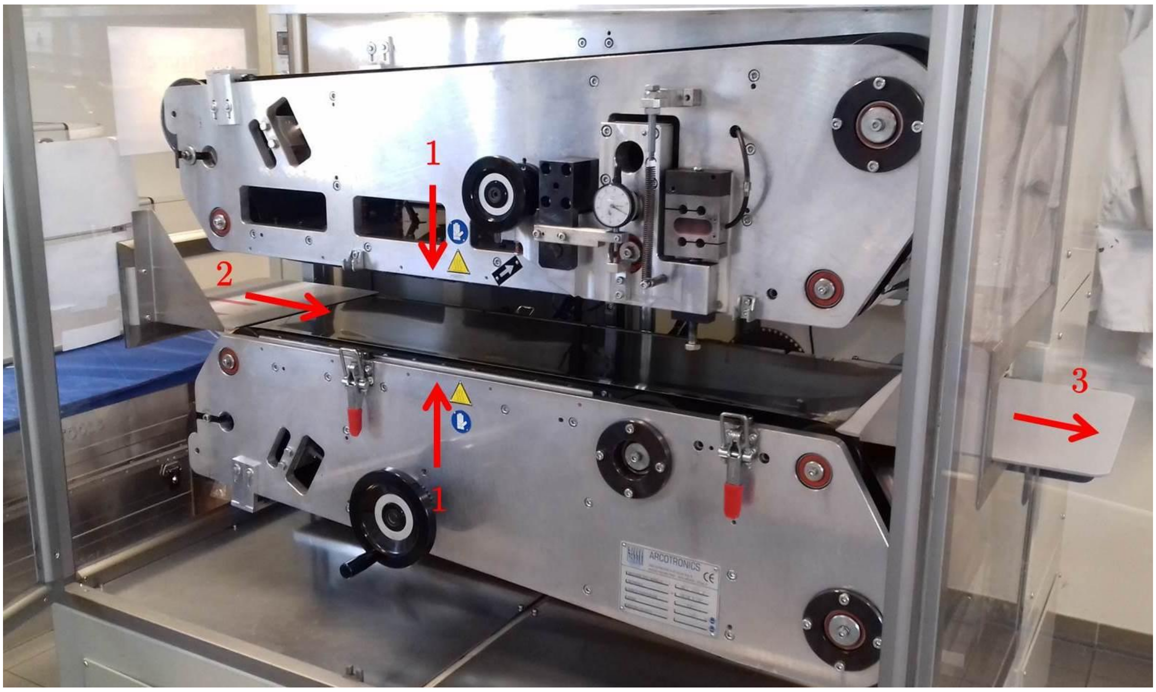

Figure 11: Image of the roll laminator. 1: Upper and lower part equipped with heating units and steel belts (closed during lamination), 2: Inserting side for non-laminated anode-separator-cathode stacks, 3: Outlet side for laminated anode-separator-cathode stacks.

As described in the caption of Figure 11, the upper and lower part of the laminator are closed during lamination and the anode-separator-cathode stack is inserted in one side. The passage through the laminator takes approximately one minute. If the result of the lamination is insufficient, the step can be repeated after readjustment of process parameters. The tightly connected stack significantly facilitates the subsequent full-cell assemblage as the components can no longer shift against each other. Furthermore, lamination should largely prevent decontacting of electrodes and separator during full-cell cycling.

The laminated stacks are connected to anode and cathode taps by ultrasonic welding and dried again before they are put into pouch bags and filled with electrolyte solution in an argon-filled glovebox. After tempering for a few hours, the full-cells are ready for the formation step and electrochemical testing. The electrochemical characterization of full-cells was carried out on a BaSyTec (Batterie System Technik) testing equipment. The full-cells are mounted on racks as shown in Figure 12. Each testing channel has its own temperature sensor for an automatic stop of the test procedure in case of overheating or fire. For complex setups several channels can be combined in Master-Slave configurations.

Figure 12: Prepared full-cells mounted on a BaSyTec rack. Each full-cell is equipped with a temperature sensor on top as a safety measure in case of battery failure.

The battery test room is air-conditioned in order to provide a constant test environment. The complementary BaSyTec software features the design of test procedures, online monitoring and data evaluation. Abort criteria can be defined by temperature, (dis-)charge duration and voltage. Figure 13 shows the user interface of the BaSyTec software for data evaluation. Depending on the desired data density, the interval of data acquisition can be defined by various criteria such as voltage steps (*e. g.* 0.05 V), electric charge (*e. g.* 0.01 mAh) or time (*e. g.* 0.1 s). Long-term cycling of batteries can result in excessive amounts of data sets and the interval of data acquisition should be selected accordingly to the scope of the experiment. Typically, high data density is favorable for detailed intra-cycle analysis and low data density should be selected for long-term performance evaluation. For simplified data evaluation, the BaSyTec software includes the option to extract only stepwise data from the complete data sets (*e. g.* endpoint data for CC/CV charge, discharge or OCV phase). Data plotting and handling can be carried out within the software, but it is also possible to export complete or stepwise data sets to various formats for further proceeding in Excel, Origin or other software.

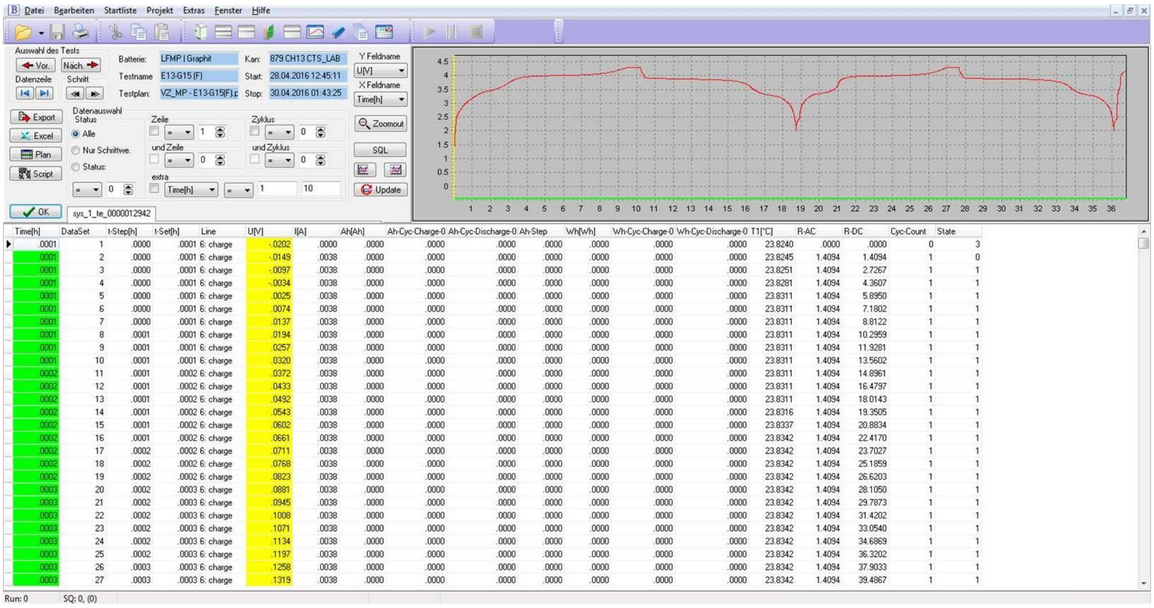

Batterie: LFMP | Graphit
Testname: E13-G15 (F)
Testplan: VZ_MP - E13-G15(F).p
Kan: 879 CH13 CTS_LAB
Start: 28.04.2016 12:45:11
Stop: 30.04.2016 01:43:25
Y Feldname: U[V]
X Feldname: Time[h]
Zeile: = 1
und Zeile: = 0
Zyklus: = 0
und Zyklus: = 0
Status: = 0
extra: Time[h] = 1 10

sys_1_te_0000012942

| Time[h] | DataSet | t-Step[h] | t-Set[h] | Line | U[V] | I[A] | Ah[Ah] | Ah-Cyc-Charge-0 | Ah-Cyc-Discharge-0 | Ah-Step | Wh[Wh] | Wh-Cyc-Charge-0 | Wh-Cyc-Discharge-0 | T1[°C] | R-AC | R-DC | Cyc-Count | State |
|---|---|---|---|---|---|---|---|---|---|---|---|---|---|---|---|---|---|---|
| .0001 | 1 | .0000 | .0001 | 6: charge | -.0202 | .0000 | .0000 | .0000 | .0000 | .0000 | .0000 | .0000 | .0000 | 23.8240 | .0000 | .0000 | 0 | 3 |
| .0001 | 2 | .0000 | .0001 | 6: charge | -.0149 | .0038 | .0000 | .0000 | .0000 | .0000 | .0000 | .0000 | .0000 | 23.8245 | 1.4094 | 1.4094 | 1 | 0 |
| .0001 | 3 | .0000 | .0001 | 6: charge | -.0097 | .0038 | .0000 | .0000 | .0000 | .0000 | .0000 | .0000 | .0000 | 23.8251 | 1.4094 | 2.7267 | 1 | 1 |
| .0001 | 4 | .0000 | .0001 | 6: charge | -.0034 | .0038 | .0000 | .0000 | .0000 | .0000 | .0000 | .0000 | .0000 | 23.8281 | 1.4094 | 4.3607 | 1 | 1 |
| .0001 | 5 | .0000 | .0001 | 6: charge | .0025 | .0038 | .0000 | .0000 | .0000 | .0000 | .0000 | .0000 | .0000 | 23.8311 | 1.4094 | 5.8950 | 1 | 1 |
| .0001 | 6 | .0000 | .0001 | 6: charge | .0074 | .0038 | .0000 | .0000 | .0000 | .0000 | .0000 | .0000 | .0000 | 23.8311 | 1.4094 | 7.1802 | 1 | 1 |
| .0001 | 7 | .0000 | .0001 | 6: charge | .0137 | .0038 | .0000 | .0000 | .0000 | .0000 | .0000 | .0000 | .0000 | 23.8311 | 1.4094 | 8.8122 | 1 | 1 |
| .0001 | 8 | .0001 | .0001 | 6: charge | .0194 | .0038 | .0000 | .0000 | .0000 | .0000 | .0000 | .0000 | .0000 | 23.8311 | 1.4094 | 10.2959 | 1 | 1 |
| .0001 | 9 | .0001 | .0001 | 6: charge | .0257 | .0038 | .0000 | .0000 | .0000 | .0000 | .0000 | .0000 | .0000 | 23.8311 | 1.4094 | 11.9281 | 1 | 1 |
| .0001 | 10 | .0001 | .0001 | 6: charge | .0320 | .0038 | .0000 | .0000 | .0000 | .0000 | .0000 | .0000 | .0000 | 23.8311 | 1.4094 | 13.5602 | 1 | 1 |
| .0002 | 11 | .0001 | .0002 | 6: charge | .0372 | .0038 | .0000 | .0000 | .0000 | .0000 | .0000 | .0000 | .0000 | 23.8311 | 1.4094 | 14.8961 | 1 | 1 |
| .0002 | 12 | .0001 | .0002 | 6: charge | .0433 | .0038 | .0000 | .0000 | .0000 | .0000 | .0000 | .0000 | .0000 | 23.8311 | 1.4094 | 16.4797 | 1 | 1 |
| .0002 | 13 | .0001 | .0002 | 6: charge | .0492 | .0038 | .0000 | .0000 | .0000 | .0000 | .0000 | .0000 | .0000 | 23.8311 | 1.4094 | 18.0143 | 1 | 1 |
| .0002 | 14 | .0001 | .0002 | 6: charge | .0543 | .0038 | .0000 | .0000 | .0000 | .0000 | .0000 | .0000 | .0000 | 23.8316 | 1.4094 | 19.3505 | 1 | 1 |
| .0002 | 15 | .0001 | .0002 | 6: charge | .0602 | .0038 | .0000 | .0000 | .0000 | .0000 | .0000 | .0000 | .0000 | 23.8337 | 1.4094 | 20.8834 | 1 | 1 |
| .0002 | 16 | .0001 | .0002 | 6: charge | .0661 | .0038 | .0000 | .0000 | .0000 | .0000 | .0000 | .0000 | .0000 | 23.8342 | 1.4094 | 22.4170 | 1 | 1 |
| .0002 | 17 | .0002 | .0002 | 6: charge | .0711 | .0038 | .0000 | .0000 | .0000 | .0000 | .0000 | .0000 | .0000 | 23.8342 | 1.4094 | 23.7027 | 1 | 1 |
| .0002 | 18 | .0002 | .0002 | 6: charge | .0768 | .0038 | .0000 | .0000 | .0000 | .0000 | .0000 | .0000 | .0000 | 23.8342 | 1.4094 | 25.1859 | 1 | 1 |
| .0002 | 19 | .0002 | .0002 | 6: charge | .0823 | .0038 | .0000 | .0000 | .0000 | .0000 | .0000 | .0000 | .0000 | 23.8342 | 1.4094 | 26.6203 | 1 | 1 |
| .0003 | 20 | .0002 | .0003 | 6: charge | .0881 | .0038 | .0000 | .0000 | .0000 | .0000 | .0000 | .0000 | .0000 | 23.8342 | 1.4094 | 28.1050 | 1 | 1 |
| .0003 | 21 | .0002 | .0003 | 6: charge | .0945 | .0038 | .0000 | .0000 | .0000 | .0000 | .0000 | .0000 | .0000 | 23.8342 | 1.4094 | 29.7873 | 1 | 1 |
| .0003 | 22 | .0002 | .0003 | 6: charge | .1008 | .0038 | .0000 | .0000 | .0000 | .0000 | .0000 | .0000 | .0000 | 23.8342 | 1.4094 | 31.4202 | 1 | 1 |
| .0003 | 23 | .0002 | .0003 | 6: charge | .1071 | .0038 | .0000 | .0000 | .0000 | .0000 | .0000 | .0000 | .0000 | 23.8342 | 1.4094 | 33.0540 | 1 | 1 |
| .0003 | 24 | .0002 | .0003 | 6: charge | .1134 | .0038 | .0000 | .0000 | .0000 | .0000 | .0000 | .0000 | .0000 | 23.8342 | 1.4094 | 34.6869 | 1 | 1 |
| .0003 | 25 | .0002 | .0003 | 6: charge | .1197 | .0038 | .0000 | .0000 | .0000 | .0000 | .0000 | .0000 | .0000 | 23.8342 | 1.4094 | 36.3202 | 1 | 1 |
| .0003 | 26 | .0003 | .0003 | 6: charge | .1258 | .0038 | .0000 | .0000 | .0000 | .0000 | .0000 | .0000 | .0000 | 23.8342 | 1.4094 | 37.9033 | 1 | 1 |
| .0003 | 27 | .0003 | .0003 | 6: charge | .1319 | .0038 | .0000 | .0000 | .0000 | .0000 | .0000 | .0000 | .0000 | 23.8342 | 1.4094 | 39.4867 | 1 | 1 |

Figure 13: BaSyTec software screen showing recorded data sets and the plot of a voltage curve.

In the following, experimental setups of the neutron experiments will be described. Although many neutron experiments can be carried out by following a standard setup and procedure, some scientific issues require an individual arrangement.

The experiment on gas evolution in LFP/graphite and LFMP/graphite cells was carried out at the ANTARES instrument at FRM II. As illustrated in Figure 14a, the pouch cell was mounted on an aluminum plate in front of the detector by using aluminum tape. The sample holder and tape only slightly attenuate the intensity of the neutron beam due to the low cross-section of aluminum. However, it was made sure that the tape only covers the sealed seam of the cell and not the electrodes or electrolyte-filled pouch cell areas in order to prevent inhomogeneous attenuation within the observed region of interest. The pouch cell was formed at C/10 and images were recorded every 30 seconds. For a precise evaluation of the gas evolution all images have to be divided by the first image. Thus, it is important that the pouch cell is fixed adequately on the aluminum plate and does not shift or become loose during *in-situ* image recording.

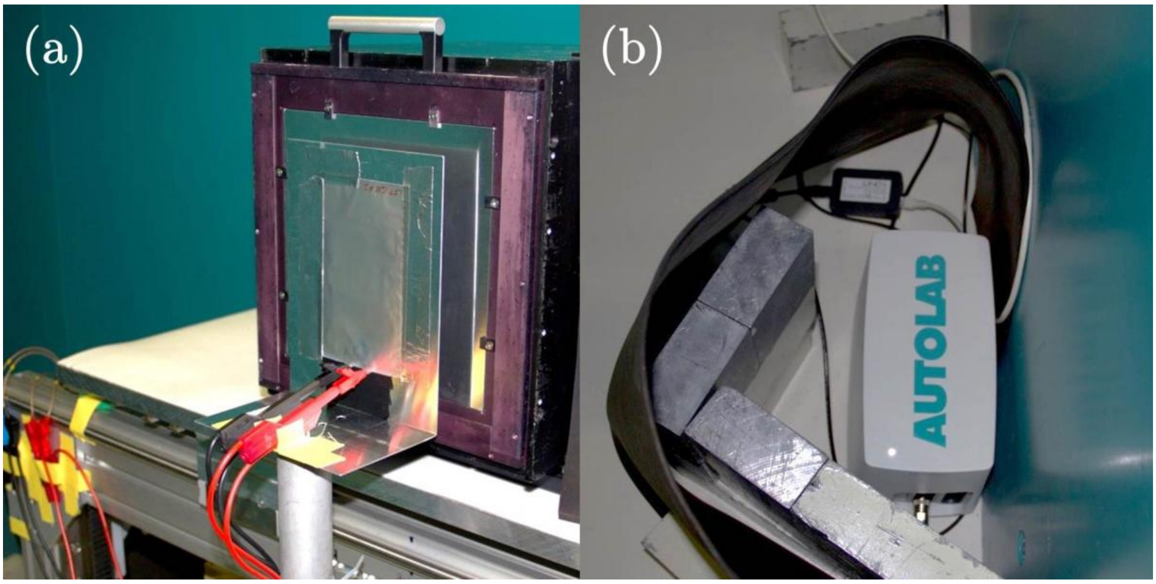

Figure 14: Experimental setup of the neutron imaging experiment: (a) Full-cell fixed with aluminum tape on an aluminum plate in front of the ANTARES detector; (b) Potentiostat surrounded by lead bricks and a boron-filled rubber mat as protection against radiation.

Figure 14b shows the potentiostat used for pouch cell charging. The potentionstat had to be positioned in close proximity to the open beam (distance approximately 1 m). As any electronic device, the potentiostat is sensitive to strong neutron and γ-radiation which may cause malfunctions. To minimize the risk of failure, the device was protected with lead bricks oriented towards the open beam. Additional protection was provided by a boron-filled rubber mat. Boron has a high cross section for neutrons and effectively attenuates their intensity.

Further improvement of the reliability of the experimental setup was reached by using an interconnected signal amplifier between the potentiostat and computer. This is recommendable since the cable length from the control room to the potentiostat is approximately 10 m.

The elemental analysis of anodes was realized at the instrument PGAA at FRM II. The samples were punched out of the extracted anodes and positioned between fine aluminum wires which were fixed in an aluminum frame as illustrated in Figure 15a. Aluminum is the appropriate sample holder material for this experimental setup since aluminum was not among the elements present in the sample and thus, does not disturb the quantification of elements to be detected. After preparation of the sample, the aluminum frame is inserted in the rotatable sample holder of the PGAA instrument as illustrated in Figure 15b. The sample holder can carry several frames and allows complete test series without interrupting the vacuum built up for measurements.

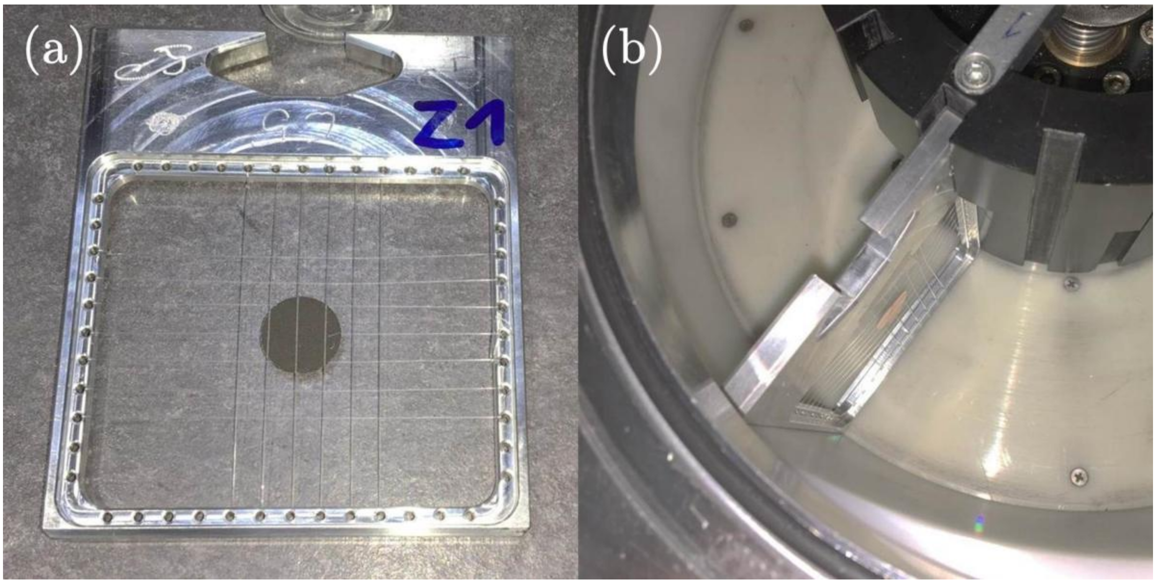

Figure 15: Sample preparation for the PGAA experiment; (a) Sample holder designed as a frame of aluminum covered with thin aluminum wires; (b) Sample chamber of the instrument PGAA. Several aluminum frames can be fixed within the chamber and measured subsequently without interrupting a measurement session.

The exact quantification of elements is best when an internal standard can be used. In the case of an anode sample, this can be achieved by knowledge of the exact weight of the Cu current collector. The amount of detected elements can then be determined by correlating element peak intensities with the Cu mass as internal standard. If the concentration of elements to be detected is very low, it is possible to measure a stack of identic samples positioned in one sample holder.

Powder diffraction of pristine and aged LFP and LFMP samples was carried out at the instrument SPODI at FRM II. Approximately 2 cm$^3$ of the powder were filled into a vanadium can with a diameter of 13 mm and a wall thickness of 0.15 mm. Vanadium has a very low coherent but relatively high incoherent cross section for neutrons [192, 193]. Hence, no vanadium Bragg peaks appear in the recorded diffraction pattern and only a low background is observable. The vanadium can is installed on the sample table of SPODI as depicted in Figure 16a. The position of the vanadium can is pointed out by the red arrow.

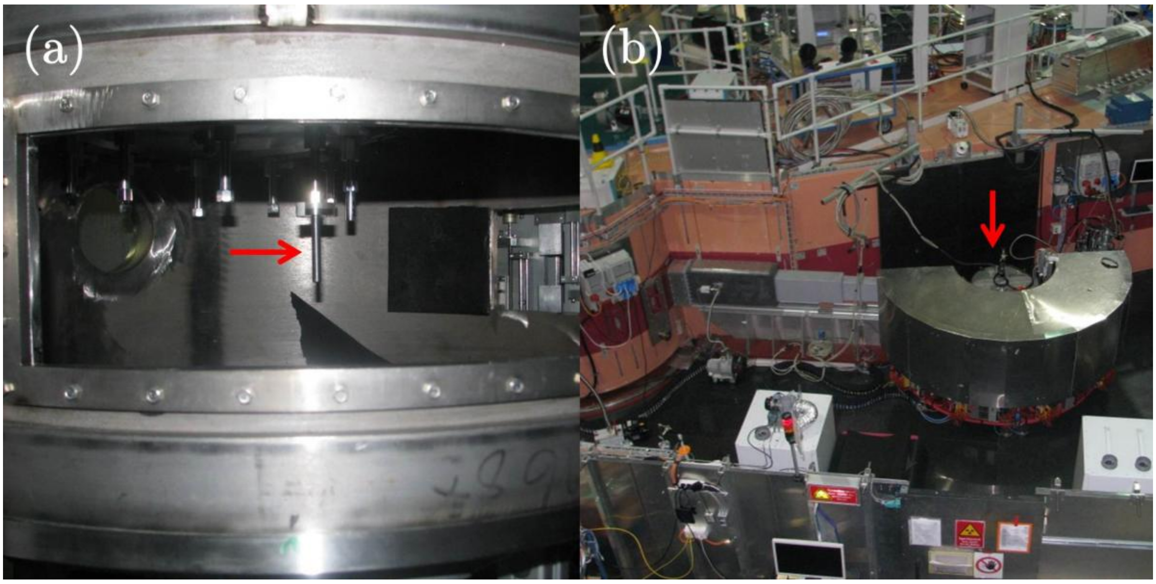

Figure 16: Experimental setup of powder diffraction at the instrument SPODI: (a) The powder is filled into a vanadium can which is fixed in the sample table; (b) Overview of sample holder and SPODI detector array.

Figure 16b gives an overview of the SPODI setup and the red arrow marks the sample table illustrated in Figure 16a, which is surrounded by the detector array. The orange casing in the background houses the incident neutron beam and the monochromator. The high take-off angle of 155° between the incident neutron beam and optical collimation is also well visible (see Figure 6 for more details).

# 3. Reprint permissions

All publications included in this thesis have been published under open access licenses. The copyright is held by the authors and no reprint permission is required from the publisher. In the following, details are given for the corresponding licenses.

Published under Attribution 4.0 International (CC BY 4.0):

- *Influence of Particle Morphologies of $LiFePO_4$ on Water- and Solvent-Based Processing and Electrochemical Properties* by B. Starke[1], S. Seidlmayer[2], S. Jankowsky[1], O. Dolotko[2], R. Gilles[2] and K.-H. Pettinger[1]
  Sustainability 2017, 9(6), 888, DOI:10.3390/su9060888

- *Ageing and Water-Based Processing of $LiFeMnPO_4$ Secondary Agglomerates and Its Effects on Electrochemical Characteristics* by B. Starke[1], S. Seidlmayer[2], O. Dolotko[2], R. Gilles[2] and K.-H. Pettinger[1]
  Energies 2017, 10, 2135; doi:10.3390/en10122135

Clear indication on the license type is on the last page of each publication.

Complete information on the license type and conditions is available on:
*https://creativecommons.org/licenses/by/4.0/legalcode*

Published under Attribution-NonCommercial-NoDerivatives 4.0 International (CC-BY-NC-ND 4.0):

- *Gas Evolution and Capacity Fading in $LiFe_xMn_{1-x}PO_4$/Graphite Cells Studied by Neutron Imaging and Neutron Induced Prompt Gamma Activation Analysis* by B. Starke[1], S. Seidlmayer[2], M. Schulz[2], A. Dinter[1], Z. Revay[2], R. Gilles[2] and K.-H. Pettinger[1]
  Journal of The Electrochemical Society, 164 (14) A3943-A3948 (2017); doi: 10.1149/2.0011802jes

Clear indication on the license type is on the first page of the publication.

Complete information on the license type and conditions is available on:
https://creativecommons.org/licenses/by-nc-nd/4.0/legalcode

# 4. Publication Summaries and Bibliographic Data

This chapter provides summaries, bibliographic data and individual contributions for the publications of this thesis.

## 4.1. Influence of Particle Morphologies of $LiFePO_4$ on Water- and Solvent-Based Processing and Electrochemical Properties

Summary of *Influence of Particle Morphologies of $LiFePO_4$ on Water- and Solvent-Based Processing and Electrochemical Properties* by B. Starke[1], S. Seidlmayer[2], S. Jankowsky[1], O. Dolotko[2], R. Gilles[2] and K.-H. Pettinger[1]

Sustainability 2017, 9(6), 888, DOI:10.3390/su9060888

[1] Technology Center for Energy, University of Applied Sciences Landshut, Am Lurzenhof 1, 84036 Landshut, Germany

[2] Heinz Maier-Leibnitz Zentrum (MLZ), Technische Universität München, 85748 Garching, Germany

In this study we investigated the influence of two different material morphologies of LFP and their effect on processing and electrochemical characteristics. Usually, active material is processed in the form of (sub-)micron primary particles (PP). By agglomeration of those particles, so-called secondary agglomerates (SA) are obtained. SA are characterized by higher bulk density.

PP and SA were processed to slurries by using water or N-methyl-2-pyrrolidone (NMP). The four different slurries were then processed to cathodes and characterized in full-cells with graphite as anode material.

Neutron and X-ray diffraction showed that no structural changes occurred upon slurry preparation. Thus, the LFP samples as such are stable in water and NMP. Electrochemical testing revealed distinct differences. At elevated C-rates PP processed with water showed a reduced discharge capacity in comparison to PP processed with NMP. The reason is very likely the loss of carbon coating due to high mechanical stress at simultaneous presence of water. Cathodes containing SA showed the opposite behavior and a slightly higher discharge capacity was found for SA processed with water. In this case, the reason is found in a better homogeneity of cathodes when the binders carboxymethyl cellulose (CMC) and styrene-butadiene rubber (SBR) are used in combination with water as a solvent. No negative effect was found upon water-based processing. The reason therefore can be found in the protective function of SA. During slurry preparation only the outer particles are exposed to high mechanical stress. The C-rate performance of NMP-based PP-cathodes was not reached by NMP- and water-based SA-cathodes. An explanation is that each SA itself represents a micro-heterogeneity in the cathode, which is in contradiction with a generally striven homogeneity.

Long-term cycling showed that water-based PP cathodes fade stronger during the first 100 cycles. Water- and NMP-based SA-cathodes showed nearly identic long-term fading and had the highest discharge capacity after 500 cycles.

Full-cells assembled with SA-cathodes revealed a lower coulomb efficiency although a lower capacity fading rate was observed during long-term cycling. It is known that the particle size distribution can affect the relation between coulomb efficiency and capacity fading. Since the LFP-particle itself were equal for PP and SA, reasons are likely to be found in the secondary structure of agglomerates.

Individual contribution:

B. S. designed and performed the electrochemical experiments, analyzed the electrochemical data and drafted the manuscript. S. S. performed XRD experiments, analyzed the data of neutron and X-ray diffraction and helped to draft the manuscript. S. J. supported the analysis and interpretation of CE data and helped to draft the manuscript. O. D. performed neutron diffraction experiments and helped to draft the manuscript. R. G. supported the analysis of X-ray and neutron diffraction data and helped to draft the manuscript. K.-H. P. supported the analysis of electrochemical data and helped to draft the manuscript.

## 4.2. Ageing and Water-Based Processing of $LiFeMnPO_4$ Secondary Agglomerates and Its Effects on Electrochemical Characteristics

Summary of *Ageing and Water-Based Processing of* $LiFeMnPO_4$ *Secondary Agglomerates and Its Effects on Electrochemical Characteristics* by B. Starke[1], S. Seidlmayer[2], O. Dolotko[2], R. Gilles[2] and K.-H. Pettinger[1]

Energies 2017, 10, 2135; doi:10.3390/en10122135

[1] Technology Center for Energy, University of Applied Sciences Landshut, Am Lurzenhof 1, 84036 Landshut, Germany

[2] Heinz Maier-Leibnitz Zentrum (MLZ), Technische Universität München, 85748 Garching, Germany

In this study, secondary agglomerates of LFMP were aged for 21 days at moderate (23 °C, 35 % relative humidity) and harsh (40 °C, 100 % relative humidity) storage conditions. The moisture uptake of the powder samples was measured via Karl-Fischer titration. For both aging conditions it was found that more the than 75 % of the moisture is adsorbed within 24 hours. The moisture content gradually increases over the following 20 days.

When the material is stored under harsh conditions the formation of acicular $Li_3PO_4$ crystals can be detected via energy dispersive X-ray spectroscopy (EDX) and inductively coupled plasma optical emission spectrometry (ICP-OES). Neutron diffraction of pristine and aged samples proved that LFMP remains unaffected by both storage conditions. Thus, the observed acicular $Li_3PO_4$ crystals are not formed under consumption of active lithium but very likely from a precursor which was used in excess during material synthesis.

Pristine and aged samples were then processed to water- and NMP-based cathodes. Via X-ray diffraction it was confirmed that LFMP is resistant to water-based processing.

Electrochemical characterization was carried out in full-cells using synthetic graphite as anode material. The initial charge capacities as well as the irreversible capacity loss (ICL) are equal for both water-and NMP-based cathodes and no effect of the initial sample aging is observable. Similar discharge capacities were observed for discharge currents in the range of 0.1 C to 1 C. At a rate of 2 C, full-cells assembled with NMP-based cathodes tend to a stronger IR-drop and slightly lower discharge capacity in comparison to water-based cathodes. This effect is more significant at 5 C. The reason for the better C-rate performance of water-based cathodes is caused by a better homogeneity of cathode constituents when the binder system CMC/SBR is used. The lower boiling point of water also allows a shorter drying period of the coated cathodes. As a consequence, the cathode constituents have less time to separate in the wet state.

Long-term cycling over 200 cycles and measurements of coulomb efficiency did not reveal any significant differences for any initial storage condition and solvent used for slurry preparation.

Additional long-term cycling of full-cells assembled with anodes containing natural graphite resulted in an approximately 5 % lower relative capacity loss after 200 cycles. Morphologic properties of graphite, such as particle size, basal-to-edge-plane ratio and crystallinity influences the full-cell performance and capacity fading. As a result of this study, the choice of anodic graphite exceeds the influence of aging and processing conditions by far. This study also confirmed the insensitivity of secondary agglomerates towards water-based processing as it has been described in our work on different LFP morphologies.

Individual contributions:

B. S. designed and performed the aging and electrochemical experiments, analyzed the data and drafted the manuscript. S. S. performed XRD experiments, analyzed the data of neutron and X-ray diffraction and helped to draft the manuscript. O. D. performed neutron diffraction experiments and helped to draft the manuscript. R. G. supported the analysis of X-ray and neutron diffraction data and helped to draft the manuscript. K.-H. P. supported the analysis of electrochemical data and helped to draft the manuscript.

## 4.3. Gas Evolution and Capacity Fading in $LiFe_xMn_{1-x}PO_4$/Graphite Cells Studied by Neutron Imaging and Neutron Induced Prompt Gamma Activation Analysis

Summary of *Gas Evolution and Capacity Fading in* $LiFe_xMn_{1-x}PO_4$*/Graphite Cells Studied by Neutron Imaging and Neutron Induced Prompt Gamma Activation Analysis* by B. Starke[1], S. Seidlmayer[2], M. Schulz[2], A. Dinter[1], Z. Revay[2], R. Gilles[2] and K.-H. Pettinger[1]

Journal of The Electrochemical Society, 164 (14) A3943-A3948 (2017);
doi: 10.1149/2.0011802jes

[1] Technology Center for Energy, University of Applied Sciences Landshut, Am Lurzenhof 1, 84036 Landshut, Germany

[2] Heinz Maier-Leibnitz Zentrum (MLZ), Technische Universität München, 85748 Garching, Germany

In this publication we used neutron imaging and prompt gamma activation analysis to study the effect of Mn-dissolution on initial gas evolution and long-term capacity fading.

As the first part of this work, neutron imaging was applied to compare the gas evolution during the initial charge of LFP/graphite and LFMP/graphite full-cells. It was found that 30 % more gas is evolved in LFMP/graphite full-cells in comparison to the system LFP/graphite. Furthermore, for both full-cells sections characterized by significantly different linear gas evolution rates could be detected over the charging process. In both cases strong gas evolution can be observed until the anode reaches a potential of approximately 0.25 V vs. $Li/Li^+$ (corresponding to the beginning formation of $LiC_{18}$), indicating major progress in the formation of the SEI-layer. In the case of LFP/graphite gassing continues at a decreased and constant rate until reaching the fully charged state. Thus, for the LFP/graphite system two distinct gassing rates are identifiable.

In contrast, LFMP/graphite exhibits an additional third linear gassing section in the cathode potential range of 3.0 V – 4.1 V vs. $Li/Li^+$. It is assumed that in this phase of the charge process dissolved Mn from LFMP migrates to the anodic graphite and gets inserted in the SEI-layer. This insertion causes continuous SEI-formation and gassing.

Long-term evaluation of Mn-dissolution and deposition on the anode surface was carried out via PGAA measurement of extracted anodes harvested from LFMP/graphite full-cells after different number of cycles. The measurements prove that Mn-dissolution decreases rapidly with increasing cycle number. Compared to values of Mn-dissolution found for oxide-type cathode active materials such as NMC, the results also state that Mn-dissolution from LFMP is relatively low.

Mn-dissolution from LFMP leads to a higher irreversible capacity loss after the formation cycle. But long-term cycling of LFP/graphite and LFMP/graphite full-cells reveals a slightly better capacity retention of LFMP/graphite full-cells, which compensates the higher formation loss after several cycles. Although Mn-dissolution can be detected for LFMP, it seems to be low enough not to trigger ongoing and measurable parasitic processes on the graphite surface.

Individual contributions:

B. S. designed and performed the electrochemical experiments, analyzed the electrochemical data, conceived and helped to carry out the neutron imaging experiment and drafted the manuscript. S. S. helped to carry out the neutron imaging experiment, supported the interpretation of data from neutron imaging and PGAA experiments and helped to draft the manuscript. M. S. carried out the neutron imaging experiment, analyzed the data and helped to draft the manuscript. A. D. supported electrochemical experiments and helped to draft the manuscript. Z. R. performed the PGAA experiment, analyzed the data and helped to draft the manuscript. R. G. supported the interpretation of neutron imaging and PGAA data and helped to draft the manuscript. K.-H. P. supported the analysis of electrochemical data and helped to draft the manuscript.

# 5. Conclusion and Outlook

This thesis focused on new aspects of aging of the intrinsically safe cathode material $LiFe_xMn_{1-x}PO_4$ in the form of $LiFePO_4$ (x = 1) and $LiFe_{0.33}Mn_{0.67}PO_4$. Neutron-based experiments provided supportive data for the understanding of potential structural changes and explanations for electrochemical behavior.

In the first part, different morphologic structures of $LiFePO_4$ were studied in the context of material processing and electrochemical properties. The morphology of primary particles was compared with secondary agglomerates, which can be regarded as a superstructure of primary particles. Secondary agglomerates are obtained by agglomeration of primary particles to large clusters. Both morphologies were processed to water- and NMP-based slurries and subsequently characterized in full-cells. Providing a discharge capacity of 92 % at 5 C, the highest C-rate capability was found for NMP-processed primary particles, while water-processed primary particles delivered 72 % discharge capacity at 5 C. Water- and NMP-processed secondary agglomerates reached 77 % and 68 % of discharge capacity at 5 C, respectively. The inversed performance of primary particles and secondary agglomerates upon water- and NMP-based processing is not explained by structural changes as such. Neutron as well as X-ray diffraction showed that lattice constants of all samples before and after processing varied only in a narrow range of 0.002 Å, 0.001 Å and 0.002 Å for *a*, *b* and *c*, respectively. Such small deviations do not indicate structural modifications implied by material processing. In case of primary particles all cathodes show a comparable homogeneity, but a partial loss of carbon coating is assumed after water-based processing as all particles are exposed to high shearing force at simultaneous contact to water explaining differences in rate capability. Regarding secondary agglomerates, it is obvious that during slurry processing the vast majority of particles is protected against mechanical stress inside the agglomerates, preventing a measurable loss of carbon coating and performance deficit. Lower C-rate performance of NMP-processed secondary agglomerates is likely caused by reduced cathode homogeneity since NMP needs a longer period of drying and undesirable mobility of constituents is prolonged. But long-term cycling resulted in identic capacity retention, indicating that this effect only comes into effect at higher C-rates. Limited C-rate of secondary agglomerates can generally be regarded as an inherent property, since each agglomerate itself represents a micro-heterogeneity. Primary particles show different characteristics in long-term cycling. After water-based processing the lowest capacity retention and strongest fading is observable. Both can be explained by partial loss of carbon coating resulting impaired kinetics and accelerated material degradation.

The second part comprised with the different characteristics of $LiFe_{0.33}Mn_{0.67}PO_4$ secondary agglomerates upon atmospheric aging (23 °C and 35 % rh, 40 °C and 100 % rh) and a combined variation in processing conditions. Aging at 40 °C/100 % rh led to the formation of acicular crystals on the surface of $LiFe_{0.33}Mn_{0.67}PO_4$ particles. EDX and ICP-OES analysis stated them to be $Li_3PO_4$. Neutron diffraction proved that no structural changes occurred after the formation of $Li_3PO_4$ indicating the excess of a synthesis precursor as source of Li. Overall, no structural modifications of $LiFe_{0.33}Mn_{0.67}PO_4$ were detectable after different aging conditions. Subsequent water- and NMP-processing of aged and pristine samples revealed similar characteristics as $LiFePO_4$ secondary agglomerates. A reduced rate capability (79.6 % at 5 C compared to 84.5 % for water-based cathodes) of NMP-processed cathodes is the result of a slightly lower homogeneity. Apart from this, no systematic influence of aging was measurable and comparable capacity retention of all full-cells was observed over 200 cycles. This states the possibility of simplified material handling in the industrial process. The study was supplemented by cycling $LiFe_{0.33}Mn_{0.67}PO_4$ cathodes with anodes prepared with synthetic flake-shaped and natural potato-shaped graphite, respectively. Full-cells containing natural graphite provided better cycling properties and a 4.9 % higher capacity retention was measured after 200 cycles in comparison to synthetic graphite. These results indicate that a variation of anodic graphite has a stronger influence than any aging or processing of $LiFe_{0.33}Mn_{0.67}PO_4$. The morphology of graphite can significantly influence the performance of batteries since parameters like crystallinity, basal-to-edge-plane ratio and pore size vary.

The third part was a comparative study on the first cycle gas evolution in $LiFePO_4$/graphite and $LiFe_{0.33}Mn_{0.67}PO_4$/graphite cells. By means of *in-operando* neutron imaging it has been found that different gas evolution rates and volumes are generated in these cell systems. In both cases the highest gas evolution rate can be observed at the beginning of charge until the anodic potential drops down to approximately 0.2 V vs. $Li/Li^+$, corresponding to an SOC of about 15 %. Normalizing the final gas volume in the $LiFePO_4$/graphite cell to 100 %, approximately 75 % of the gas has been generated at this point. The gas evolution rate in the $LiFePO_4$/graphite cell then remains constant until SOC = 100 %. Regarding the $LiFe_{0.33}Mn_{0.67}PO_4$/graphite cell, almost 90 % of the overall gas volume observed for the $LiFePO_4$/graphite are generated when the anodic potential reaches 0.2 V vs. $Li/Li^+$. Thus, a stronger gas evolution can be stated and Mn in $LiFe_{0.33}Mn_{0.67}PO_4$ seems to be responsible for this behavior as it is the only variation between both cells. The gas evolution rate in the $LiFe_{0.33}Mn_{0.67}PO_4$/graphite cell decreases after the anode reaches 0.2 V vs. $Li/Li^+$, but it is still elevated. When reaching the cathode potential of 4.1 V vs. $Li/Li^+$, gas evolution is equal to the rate observed for the $LiFePO_4$/graphite cell. The phase between the anode potential of 0.2 V vs. $Li/Li^+$ and the cathode potential of 4.1 V vs. $Li/Li^+$, which corresponds to the beginning $Mn^{2+}/Mn^{3+}$ redox plateau, is characteristic for the $LiFe_{0.33}Mn_{0.67}PO_4$/graphite cell and the final gas volume is 30 % higher in comparison to the $LiFePO_4$/graphite cell. It is very likely that Mn-dissolution and migration to the anodic graphite is responsible for the elevated gas evolution since it disturbs the formation of the SEI-layer. However, it remains unanswered in how far the beginning $Mn^{2+}/Mn^{3+}$ redox plateau and decreasing gas evolution rate are correlated. A more detailed investigation of Mn-dissolution via PGAA has been included in this study and it was found that Mn-dissolution mainly takes place in the beginning and decreases strongly with ongoing cycling. Overall, the extent of Mn-dissolution is quite moderate in comparison to values observable for Mn-containing layered oxides.

Concluding, the results of this work demonstrate the suitability of $LiFe_{0.33}Mn_{0.67}PO_4$ and $LiFePO_4$ secondary agglomerates for water-based and thus, environmentally friendly cathode manufacturing. Consequently both materials hold the potential to replace commonly used organic solvents such as NMP, which requires cost-intensive exhaust treatments and protective measures for workers due to its toxicity. Furthermore, material handling can be simplified since temporary storage and processing in moist atmosphere did not result in reduced performance. Dry room conditions are not mandatory as long as coated electrodes are dried thoroughly before battery assemblage. These results are of particular interest for Mn-rich $LiFe_xMn_{1-x}PO_4$ as it provides a higher operating voltage and energy density in comparison to Mn-free $LiFePO_4$.

# References

1. Armand, M.B. Intercalation Electrodes. In *Materials for Advanced Batteries*; Murphy, D.W., Broadhead, J., Steele, B.C.H., Eds.; Springer US: Boston, MA, 1980; pp 145–161.
2. Blomgren, G.E. The Development and Future of Lithium Ion Batteries. *Journal of The Electrochemical Society* 2016, *164*, A5019-A5025, doi:10.1149/2.0251701jes.
3. Hunter, J.C. Preparation of a new crystal form of manganese dioxide: Λ-$MnO_2$. *Journal of Solid State Chemistry* 1981, *39*, 142–147, doi:10.1016/0022-4596(81)90323-6.
4. Mizushima, K.; Jones, P.C.; Wiseman, P.J.; Goodenough, J.B. LixCoO2 (0<x<-1): A new cathode material for batteries of high energy density. *Materials Research Bulletin* 1980, *15*, 783–789, doi:10.1016/0025-5408(80)90012-4.
5. Fong, R. Studies of Lithium Intercalation into Carbons Using Nonaqueous Electrochemical Cells. *Journal of The Electrochemical Society* 1990, *137*, 2009, doi:10.1149/1.2086855.
6. Yoshino K., Sanechika, Nakajima T. “Secondary battery”, U. S. Pat. 4,668,595, 26 May (1987).
7. Nishi, Y. The development of lithium ion secondary batteries. In *1996 Symposium on VLSI Circuits. Digest of Technical Papers.* 1996 Symposium on VLSI Circuits. Digest of Technical Papers, Honolulu, HI, USA, 13-15 June 1996; Widerkehr & Associates, 1996; pp 88–89.
8. Goodenough, J.B.; Park, K.-S. The Li-ion rechargeable battery: A perspective. *Journal of the American Chemical Society* 2013, *135*, 1167–1176, doi:10.1021/ja3091438.
9. Yoshio, M.; Brodd, R.J.; Kozawa, A. *Lithium-Ion Batteries;* Springer New York: New York, NY, 2009.
10. Lopez, J.; Gonzalez, M.; Viera, J.C.; Blanco, C. Fast-charge in lithium-ion batteries for portable applications. In *2004 10th International Workshop on Computational Electronics (IEEE Cat. No.04EX915).* INTELEC 26th Annual International Telecommunications Energy Conference, Chicago, IL, USA, 19-23 Sept. 2004; IEEE, 2004; pp 19–24.

11. Guo, S.; Li, Q.; Liu, P.; Chen, M.; Zhou, H. Environmentally stable interface of layered oxide cathodes for sodium-ion batteries. *Nature communications* 2017, *8*, 135, doi:10.1038/s41467-017-00157-8.
12. Hausbrand, R.; Cherkashinin, G.; Ehrenberg, H.; Gröting, M.; Albe, K.; Hess, C.; Jaegermann, W. Fundamental degradation mechanisms of layered oxide Li-ion battery cathode materials: Methodology, insights and novel approaches. *Materials Science and Engineering: B* 2015, *192*, 3–25, doi:10.1016/j.mseb.2014.11.014.
13. Balakrishnan, P.G.; Ramesh, R.; Prem Kumar, T. Safety mechanisms in lithium-ion batteries. *Journal of Power Sources* 2006, *155*, 401–414, doi:10.1016/j.jpowsour.2005.12.002.
14. Goertz, R. Gefahrenabwehr bei der Zersetzung von Li-Ionen-Akkus - Sachstand. Available online: http://www.fahrzeugsicherheit-berlin.de/cms/wp-content/uploads/Goertz_Batteriesicherheit-und-Gefahrenabwehr.pdf (accessed on 03.05.2018).
15. Lamp, P. Anforderungen an Batterien für die Elektromobilität. In *Handbuch Lithium-Ionen-Batterien*; Korthauer, R., Ed.; Springer Berlin Heidelberg: Berlin, Heidelberg, 2013; pp 393–415.
16. Schäfer, T. Sicherheit, Brandsicherheit und Umweltschutz im Fokus: DryCloud Li-Ionen Batterien – Made in Germany. Available online: http://www.envites.de/images/pdf/LiThiumIonenTechnologie_Stand_und_Ausblick.pdf (accessed on 03.05.2018).
17. Matadi, B.P.; Geniès, S.; Delaille, A.; Chabrol, C.; Vito, E.d.; Bardet, M.; Martin, J.-F.; Daniel, L.; Bultel, Y. Irreversible Capacity Loss of Li-Ion Batteries Cycled at Low Temperature Due to an Untypical Layer Hindering Li Diffusion into Graphite Electrode. *Journal of The Electrochemical Society* 2017, *164*, A2374-A2389, doi:10.1149/2.0491712jes.
18. Yang, X.-G.; Leng, Y.; Zhang, G.; Ge, S.; Wang, C.-Y. Modeling of lithium plating induced aging of lithium-ion batteries: Transition from linear to nonlinear aging. *Journal of Power Sources* 2017, *360*, 28–40, doi:10.1016/j.jpowsour.2017.05.110.
19. Love, C.T.; Baturina, O.A.; Swider-Lyons, K.E. Observation of Lithium Dendrites at Ambient Temperature and Below. *ECS Electrochemistry Letters* 2014, *4*, A24-A27, doi:10.1149/2.0041502eel.
20. An, S.J.; Li, J.; Daniel, C.; Mohanty, D.; Nagpure, S.; Wood, D.L. The state of understanding of the lithium-ion-battery graphite solid electrolyte interphase (SEI) and its relationship to formation cycling. *Carbon* 2016, *105*, 52–76, doi:10.1016/j.carbon.2016.04.008.

21. Cheng, X.-B.; Zhang, R.; Zhao, C.-Z.; Wei, F.; Zhang, J.-G.; Zhang, Q. A Review of Solid Electrolyte Interphases on Lithium Metal Anode. *Advanced science (Weinheim, Baden-Wurttemberg, Germany)* 2016, *3*, 1500213, doi:10.1002/advs.201500213.
22. Aurbach, D. The Study of Electrolyte Solutions Based on Ethylene and Diethyl Carbonates for Rechargeable Li Batteries. *Journal of The Electrochemical Society* 1995, *142*, 2882, doi:10.1149/1.2048659.
23. Zhang, S.S.; Jow, T.R.; Amine, K.; Henriksen, G.L. $LiPF_6$–EC–EMC electrolyte for Li-ion battery. *Journal of Power Sources* 2002, *107*, 18–23, doi:10.1016/S0378-7753(01)00968-5.
24. Li, Q.; Chen, J.; Fan, L.; Kong, X.; Lu, Y. Progress in electrolytes for rechargeable Li-based batteries and beyond. *Green Energy & Environment* 2016, *1*, 18–42, doi:10.1016/j.gee.2016.04.006.
25. Xu, K. Nonaqueous Liquid Electrolytes for Lithium-Based Rechargeable Batteries. *Chemical Reviews* 2004, *104*, 4303–4418, doi:10.1021/cr030203g.
26. Hess, S.; Wohlfahrt-Mehrens, M.; Wachtler, M. Flammability of Li-Ion Battery Electrolytes: Flash Point and Self-Extinguishing Time Measurements. *Journal of The Electrochemical Society* 2014, *162*, A3084-A3097, doi:10.1149/2.0121502jes.
27. Wang, Q.; Ping, P.; Zhao, X.; Chu, G.; Sun, J.; Chen, C. Thermal runaway caused fire and explosion of lithium ion battery. *Journal of Power Sources* 2012, *208*, 210–224, doi:10.1016/j.jpowsour.2012.02.038.
28. Auxiliary Power Unit Battery Fire, Japan Airlines Boeing 787-8, JA829J, Boston, Massachusetts; NTSB/AIR-14/01. National Transportation Safety Board: Washington, DC, USA, 2014. Available online: http://www.ntsb.gov/investigations/AccidentReports/Reports/AIR1401.pdf (accessed on 05.02.2018).
29. Accident: ANA B788 near Takamatsu on Jan 16th 2013, battery problem and burning smell on board (including JAL Boston, Ethiopian London and JAL Tokyo events). Available online: http://avherald.com/h?article=45c377c5&opt=0 (accessed on 05.02.2018).
30. International Air Transport Association (IATA). Lithium Batteries as Cargo in 2016 Update III, 2016. Available online: http://www.iata.org/whatwedo/cargo/dgr/Documents/lithium-battery-update.pdf (accessed on 05.02.2018).
31. Samsung Recalls Galaxy Note7 Smartphones Due to Serious Fire and Burn Hazards. Available online: https://www.cpsc.gov/Recalls/2016/Samsung-Recalls-Galaxy-Note7-Smartphones/#remedy (accessed on 05.02.2018).

32. Passenger information on Samsung Galaxy Note 7. Available online: https://www.easa.europa.eu/newsroom-and-events/news/passenger-information-samsung-galaxy-note-7 (accessed on 05.02.2018).
33. FAA Statement on Samsung Galaxy Note 7 Devices. Available online: https://www.faa.gov/news/updates/?newsId=86424 (accessed on 05.02.2018).
34. Samsung Expands Recall to All Galaxy Note7 Devices. Available online: http://www.samsung.com/us/note7recall/ (accessed on 05.02.2018).
35. Samsung Announces Cause of Galaxy Note7 Incidents in Press Conference. Available online: https://news.samsung.com/us/Samsung-Electronics-Announces-Cause-of-Galaxy-Note7-Incidents-in-Press-Conference (accessed on 05.02.2018).
36. Naumann, M.; Karl, R.C.; Truong, C.N.; Jossen, A.; Hesse, H.C. Lithium-ion Battery Cost Analysis in PV-household Application. *Energy Procedia* 2015, *73*, 37–47, doi:10.1016/j.egypro.2015.07.555.
37. Rodrigues, S.; Faria, F.; Ivaki, A.R.; Cafôfo, N.; Chen, X.; Mata-Lima, H.; Morgado-Dias, F. TESLA POWERWALL: ANALYSIS OF ITS USE IN PORTUGAL AND UNITED STATES. *International Journal of Power and Energy Systems* 2016, *36, doi:*10.2316/Journal.203.2016.1.203-6218.
38. Energy Storage Safety Strategic Plan, U.S. Department of Energy. Available online: https://energy.gov/sites/prod/files/2014/12/f19/OE%20Safety%20Strategic%20Plan%20December%202014.pdf (accessed on 06.02.2018).
39. Lithium Ion Battery Energy Storage System Fires. Available online: https://www.nfpa.org/-/media/Files/News-and-Research/Resources/Research-Foundation/Symposia/2016-SUPDET/2016-Papers/SUPDET2016BlumLong.ashx?la=en&hash=7943B59D964985A57B8111FD24A2AC3BD608863E (accessed on 06.02.2018).
40. Battery sector fights fire-risk rules. Available online: https://www.theaustralian.com.au/national-affairs/climate/battery-sector-fights-firerisk-rules/news-story/437830c088190aae9dbb120dd9810e1c (accessed on 06.02.2018).
41. German solar industry to share safety notes on lithium-ion batteries. Available online: https://www.energy-storage.news/news/german-solar-industry-to-share-safety-notes-on-lithium-ion-batteries (accessed on 06.02.2018).
42. Wang, X.; Adelmann, P.; Reindl, T. Use of $LiFePO_4$ Batteries in Stand-Alone Solar System. *Energy Procedia* 2012, *25*, 135–140, doi:10.1016/j.egypro.2012.07.018.
43. Perkins, D. *Mineralogy*, 3rd ed.; Prentice Hall: Boston, 2011.

44. Padhi, A.K. Phospho-olivines as Positive-Electrode Materials for Rechargeable Lithium Batteries. *Journal of The Electrochemical Society* 1997, *144*, 1188, doi:10.1149/1.1837571.
45. Zhou, F.; Cococcioni, M.; Kang, K.; Ceder, G. The Li intercalation potential of $LiMPO_4$ and $LiMSiO_4$ olivines with M=Fe, Mn, Co, Ni. *Electrochemistry Communications* 2004, *6*, 1144–1148, doi:10.1016/j.elecom.2004.09.007.
46. Amine, K. Olivine $LiCoPO_4$ as 4.8 V Electrode Material for Lithium Batteries. *Electrochemical and Solid-State Letters* 1999, *3*, 178, doi:10.1149/1.1390994.
47. Wolfenstine, J.; Allen, J. Ni3+/Ni2+ redox potential in LiNiPO4. *Journal of Power Sources* 2005, *142*, 389–390, doi:10.1016/j.jpowsour.2004.11.024.
48. Xu, K.; Angell, C.A. Sulfone-Based Electrolytes for Lithium-Ion Batteries. *J. Electrochem. Soc.* 2002, *149*, A920, doi:10.1149/1.1483866.
49. Kim, J.-H.; Pieczonka, N.P.W.; Yang, L. Challenges and approaches for high-voltage spinel lithium-ion batteries. *Chemphyschem : a European journal of chemical physics and physical chemistry* 2014, *15*, 1940–1954, doi:10.1002/cphc.201400052.
50. Wu, Y. *Lithium-ion batteries. Fundamentals and applications;* CRC Press: Boca Raton, 2015.
51. Yamada, A.; Takei, Y.; Koizumi, H.; Sonoyama, N.; Kanno, R.; Itoh, K.; Yonemura, M.; Kamiyama, T. Electrochemical, Magnetic, and Structural Investigation of the $Li_x(Mn_yFe_{1-y})PO_4$ Olivine Phases. *Chemistry of Materials* 2006, *18*, 804–813, doi:10.1021/cm051861f.
52. Ait-Salah, A.; Dodd, J.; Mauger, A.; Yazami, R.; Gendron, F.; Julien, C.M. Structural and Magnetic Properties of $LiFePO_4$ and Lithium Extraction Effects. *Zeitschrift für anorganische und allgemeine Chemie* 2006, *632*, 1598–1605, doi:10.1002/zaac.200600090.
53. Julien, C.; Mauger, A.; Zaghib, K.; Groult, H. Comparative Issues of Cathode Materials for Li-Ion Batteries. *Inorganics* 2014, *2*, 132–154, doi:10.3390/inorganics2010132.
54. Wang, C.; Hong, J. Ionic/Electronic Conducting Characteristics of $LiFePO_4$ Cathode Materials. *Electrochemical and Solid-State Letters* 2007, *10*, A65, doi:10.1149/1.2409768.
55. Shi, S.; Liu, L.; Ouyang, C.; Wang, D.-s.; Wang, Z.; Chen, L.; Huang, X. Enhancement of electronic conductivity of $LiFePO_4$ by Cr doping and its identification by first-principles calculations. *Physical Review B* 2003, *68*, 694, doi:10.1103/PhysRevB.68.195108.

56. Zhang, W.-J. Structure and performance of $LiFePO_4$ cathode materials: A review. *Journal of Power Sources* 2011, *196*, 2962–2970, doi:10.1016/j.jpowsour.2010.11.113.
57. Xu, Y.-N.; Ching, W.Y.; Chiang, Y.-M. Comparative studies of the electronic structure of $LiFePO_4$, $FePO_4$, $Li_3PO_4$, $LiMnPO_4$, $LiCoPO_4$, and $LiNiPO_4$. *Journal of Applied Physics* 2004, *95*, 6583–6585, doi:10.1063/1.1667422.
58. Park, M.; Zhang, X.; Chung, M.; Less, G.B.; Sastry, A.M. A review of conduction phenomena in Li-ion batteries. *Journal of Power Sources* 2010, *195*, 7904–7929, doi:10.1016/j.jpowsour.2010.06.060.
59. Jung, S.; Jung, H.-Y. Charge/discharge characteristics of Li-ion batteries with two-phase active materials: A comparative study of $LiFePO_4$ and $LiCoO_2$ cells. *International Journal of Energy Research* 2016, *40*, 1541–1555, doi:10.1002/er.3540.
60. Borong Wu, Yonghuan Ren and Ning Li (2011), LiFePO4 Cathode Material, Electric Vehicles, The Benefits and Barriers, Dr. Seref Soylu (Ed.), ISBN: 978-953- 307-287-6, InTech. Available online: http://www.intechopen.com/books/electric-vehicles-t he-benefits-and-barriers/lifepo4-cathode-material (accessed on 15.02.2018).
61. Drezen, T.; Kwon, N.-H.; Bowen, P.; Teerlinck, I.; Isono, M.; Exnar, I. Effect of particle size on $LiMnPO_4$ cathodes. *Journal of Power Sources* 2007, *174*, 949–953, doi:10.1016/j.jpowsour.2007.06.203.
62. Martha, S.K.; Markovsky, B.; Grinblat, J.; Gofer, Y.; Haik, O.; Zinigrad, E.; Aurbach, D.; Drezen, T.; Wang, D.; Deghenghi, G.*; et al.* $LiMnPO_4$ as an Advanced Cathode Material for Rechargeable Lithium Batteries. *Journal of The Electrochemical Society* 2009, *156*, A541, doi:10.1149/1.3125765.
63. Yamada, A.; Hosoya, M.; Chung, S.-C.; Kudo, Y.; Hinokuma, K.; Liu, K.-Y.; Nishi, Y. Olivine-type cathodes. *Journal of Power Sources* 2003, *119-121*, 232–238, doi:10.1016/S0378-7753(03)00239-8.
64. Chen, G.; Shukla, A.K.; Song, X.; Richardson, T.J. Improved kinetics and stabilities in Mg-substituted $LiMnPO_4$. *Journal of Materials Chemistry* 2011, *21*, 10126, doi:10.1039/C0JM04230G.
65. Baba, Y. Thermal stability of $Li_xCoO_2$ cathode for lithium ion battery. *Solid State Ionics* 2002, *148*, 311–316, doi:10.1016/S0167-2738(02)00067-X.
66. Dahn, J.R.; FULLER, E.; OBROVAC, M.; VONSACKEN, U. Thermal stability of $Li_xCoO_2$, $Li_xNiO_2$ and $\lambda$-$MnO_2$ and consequences for the safety of Li-ion cells. *Solid State Ionics* 1994, *69*, 265–270, doi:10.1016/0167-2738(94)90415-4.

67. Furushima, Y.; Yanagisawa, C.; Nakagawa, T.; Aoki, Y.; Muraki, N. Thermal stability and kinetics of delithiated $LiCoO_2$. *Journal of Power Sources* 2011, *196*, 2260–2263, doi:10.1016/j.jpowsour.2010.09.076.
68. Gabrisch, H.; Kombolias, M.; Mohanty, D. Thermal decomposition of $Li_xCoO_2$ monitored by electron energy loss spectroscopy and magnetic susceptibility measurements. *Solid State Ionics* 2010, *181*, 71–78, doi:10.1016/j.ssi.2009.12.007.
69. Gabrisch, H.; Ozawa, Y.; Yazami, R. Crystal structure studies of thermally aged $LiCoO_2$ and $LiMn_2O_4$ cathodes. *Electrochimica Acta* 2006, *52*, 1499–1506, doi:10.1016/j.electacta.2006.02.050.
70. Yamaki, J.-i.; Baba, Y.; Katayama, N.; Takatsuji, H.; Egashira, M.; Okada, S. Thermal stability of electrolytes with $Li_xCoO_2$ cathode or lithiated carbon anode. *Journal of Power Sources* 2003, *119-121*, 789–793, doi:10.1016/S0378-7753(03)00254-4.
71. Spotnitz, R.; Franklin, J. Abuse behavior of high-power, lithium-ion cells. *Journal of Power Sources* 2003, *113*, 81–100, doi:10.1016/S0378-7753(02)00488-3.
72. Yamaki, J. Thermal stability of graphite anode with electrolyte in lithium-ion cells. *Solid State Ionics* 2002, *148*, 241–245, doi:10.1016/S0167-2738(02)00060-7.
73. Belharouak, I.; Sun, Y.-K.; Liu, J.; Amine, K. $Li(Ni_{1/3}Co_{1/3}Mn_{1/3})O_2$ as a suitable cathode for high power applications. *Journal of Power Sources* 2003, *123*, 247–252, doi:10.1016/S0378-7753(03)00529-9.
74. Arai, H.; Tsuda, M.; Saito, K.; Hayashi, M.; Sakurai, Y. Thermal Reactions Between Delithiated Lithium Nickelate and Electrolyte Solutions. *Journal of The Electrochemical Society* 2002, *149*, A401, doi:10.1149/1.1452114.
75. Noh, H.-J.; Youn, S.; Yoon, C.S.; Sun, Y.-K. Comparison of the structural and electrochemical properties of layered $Li[Ni_xCo_yMn_z]O_2$ ($x = 1/3$, 0.5, 0.6, 0.7, 0.8 and 0.85) cathode material for lithium-ion batteries. *Journal of Power Sources* 2013, *233*, 121–130, doi:10.1016/j.jpowsour.2013.01.063.
76. Joachin, H.; Kaun, T.D.; Zaghib, K.; Prakash, J. Electrochemical and Thermal Studies of Carbon-Coated $LiFePO_4$ Cathode. *Journal of The Electrochemical Society* 2009, *156*, A401, doi:10.1149/1.3106121.
77. Jiang, J.; Dahn, J.R. ARC studies of the thermal stability of three different cathode materials: $LiCoO_2$ ; $Li[Ni_{0.1}Co_{0.8}Mn_{0.1}]O_2$ ; and $LiFePO_4$, in $LiPF_6$ and LiBoB EC/DEC electrolytes. *Electrochemistry Communications* 2004, *6*, 39–43, doi:10.1016/j.elecom.2003.10.011.
78. Zaghib, K.; Dubé, J.; Dallaire, A.; Galoustov, K.; Guerfi, A.; Ramanathan, M.; Benmayza, A.; Prakash, J.; Mauger, A.; Julien, C.M. Enhanced thermal safety

and high power performance of carbon-coated $LiFePO_4$ olivine cathode for Li-ion batteries. *Journal of Power Sources* 2012, *219*, 36–44, doi:10.1016/j.jpowsour.2012.05.018.

79. Yamada, A.; Chung, S.C.; Hinokuma, K. Optimized $LiFePO_4$ for Lithium Battery Cathodes. *Journal of The Electrochemical Society* 2001, *148*, A224, doi:10.1149/1.1348257.
80. Yuan, L.-X.; Wang, Z.-H.; Zhang, W.-X.; Hu, X.-L.; Chen, J.-T.; Huang, Y.-H.; Goodenough, J.B. Development and challenges of $LiFePO_4$ cathode material for lithium-ion batteries. *Energy Environ. Sci.* 2011, *4*, 269–284, doi:10.1039/C0EE00029A.
81. Takahashi, M.; Ohtsuka, H.; Akuto, K.; Sakurai, Y. Confirmation of Long-Term Cyclability and High Thermal Stability of $LiFePO_4$ in Prismatic Lithium-Ion Cells. *Journal of The Electrochemical Society* 2005, *152*, A899, doi:10.1149/1.1874693.
82. United States Geological Survey, Mineral Commodity Summaries 2017 - Iron and Steel. Available online: https://minerals.usgs.gov/minerals/pubs/commodity/iron_&_steel/mcs-2017-feste.pdf (accessed on 22.02.2018).
83. United States Geological Survey, Mineral Commodity Summaries 2017 - Manganese. Available online: https://minerals.usgs.gov/minerals/pubs/commodity/manganese/mcs-2017-manga.pdf (accessed on 22.02.2018).
84. United States Geological Survey, Mineral Commodity Summaries 2017 - Cobalt. Available online: https://minerals.usgs.gov/minerals/pubs/commodity/cobalt/mcs-2017-cobal.pdf (accessed on 22.02.2018).
85. Wang, J.; Sun, X. Olivine $LiFePO_4$: The remaining challenges for future energy storage. *Energy & Environmental Science* 2015, *8*, 1110–1138, doi:10.1039/c4ee04016c.
86. Nitta, N.; Wu, F.; Lee, J.T.; Yushin, G. Li-ion battery materials: Present and future. *Materials Today* 2015, *18*, 252–264, doi:10.1016/j.mattod.2014.10.040.
87. http://www.sxt-scooters.de/en/Scooter-models/SXT500-EEC-electric-scooter-no-helmet-duty.html (accessed on 23.02.2018).
88. https://bmsbattery.com/ebike-battery/870-72v15ah-40152-lifepo4-battery-24-cells-ebike-battery-pack-battery.html (accessed on 23.02.2018).
89. http://www.batteryspace.com/Nanophosphate-LiFePO4-26650-Power-Sports-Starter-Battery-12V-2.5Ah.aspx (accessed on 23.02.2018).

90. The 2012 CODA All-Electric Vehicle: Ready to Roll. Available online: http://www.calstart.org/News_and_Publications/CALSTART-Current-Newsletter/March_April_2012_Current/CODA_March_2012_Current.aspx (accessed on 22.03.2018).
91. The Lightweight Marine Battery That Boosts Your Boat's Performance. Available online: http://www.relionbattery.com/blog/the-lightweight-marine-battery-that-boosts-your-boat-s-performance (accessed on 23.02.2018).
92. *IECON 2013 - 39th Annual Conference of the IEEE Industrial Electronics Society.* IECON 2013 - 39th Annual Conference of the IEEE Industrial Electronics Society, Vienna, Austria, 10.11.2013 - 13.11.2013; IEEE, 2013.
93. Choi, D.; Wang, D.; Viswanathan, V.V.; Bae, I.-T.; Wang, W.; Nie, Z.; Zhang, J.-G.; Graff, G.L.; Liu, J.; Yang, Z.*; et al.* Li-ion batteries from $LiFePO_4$ cathode and anatase/graphene composite anode for stationary energy storage. *Electrochemistry Communications* 2010, *12*, 378–381, doi:10.1016/j.elecom.2009.12.039.
94. Kim, J.-H.; Woo, S.C.; Park, M.-S.; Kim, K.J.; Yim, T.; Kim, J.-S.; Kim, Y.-J. Capacity fading mechanism of $LiFePO_4$-based lithium secondary batteries for stationary energy storage. *Journal of Power Sources* 2013, *229*, 190–197, doi:10.1016/j.jpowsour.2012.12.024.
95. Swierczynski, M.; Stroe, D.; Stan, A.-I.; Teodorescu, R. The lifetime of the $LiFePO_4$/C battery energy storage system when used for smoothing of the wind power plant variations. In *IECON 2013 - 39th Annual Conference of the IEEE Industrial Electronics Society.* IECON 2013 - 39th Annual Conference of the IEEE Industrial Electronics Society, Vienna, Austria, 10.11.2013 - 13.11.2013; IEEE, 2013; pp 6825–6830.
96. Wang, W.; Choi, D.; Yang, Z. Li-Ion Battery with $LiFePO_4$ Cathode and $Li_4Ti_5O_{12}$ Anode for Stationary Energy Storage. *Metallurgical and Materials Transactions A* 2013, *44*, 21–25, doi:10.1007/s11661-012-1284-4.
97. Xu, T.; Wang, W.; Gordin, M.L.; Wang, D.; Choi, D. Lithium-ion batteries for stationary energy storage. *JOM: The Journal of the Minerals* 2010, *62*, 24–30, doi:10.1007/s11837-010-0131-6.
98. BYD Introduces New Safe and Stable Residential and Commercial Energy Storage Systems in Australia. Available online: http://www.byd.com/news/news-387.html (accessed on 23.02.2018).
99. LiFeMnPo4 batteries for solar power storage. Available online: http://www.innopower.de/en/products/lifemnpo4-batteries-for-solar-power-storage (accessed online 23.02.2018).

100. Cuisinier, M.; Martin, J.-F.; Dupré, N.; Yamada, A.; Kanno, R.; Guyomard, D. Moisture driven aging mechanism of $LiFePO_4$ subjected to air exposure. *Electrochemistry Communications* 2010, *12*, 238–241, doi:10.1016/j.elecom.2009.12.003.

101. Guo, X.; Zuo, J.; Zhan, H.; Zhou, Y. Storage Stability of $LiFePO_4$/C in Humid-hot Air. *Chinese Journal of Chemistry* 2011, *29*, 2337–2344, doi:10.1002/cjoc.201180400.

102. Martin, J.F.; Yamada, A.; Kobayashi, G.; Nishimura, S.-i.; Kanno, R.; Guyomard, D.; Dupré, N. Air Exposure Effect on $LiFePO_4$. *Electrochemical and Solid-State Letters* 2008, *11*, A12, doi:10.1149/1.2801016.

103. Hamelet, S.; Gibot, P.; Casas-Cabanas, M.; Bonnin, D.; Grey, C.P.; Cabana, J.; Leriche, J.-B.; Rodriguez-Carvajal, J.; Courty, M.; Levasseur, S.*; et al.* The effects of moderate thermal treatments under air on $LiFePO_4$-based nano powders. *Journal of Materials Chemistry* 2009, *19*, 3979, doi:10.1039/b901491h.

104. Zaghib, K.; Dontigny, M.; Charest, P.; Labrecque, J.F.; Guerfi, A.; Kopec, M.; Mauger, A.; Gendron, F.; Julien, C.M. Aging of $LiFePO_4$ upon exposure to $H_2O$. *Journal of Power Sources* 2008, *185*, 698–710, doi:10.1016/j.jpowsour.2008.08.028.

105. Porcher, W.; Moreau, P.; Lestriez, B.; Jouanneau, S.; Le Cras, F.; Guyomard, D. Stability of $LiFePO_4$ in water and consequence on the Li battery behaviour. *Ionics* 2008, *14*, 583–587, doi:10.1007/s11581-008-0215-2.

106. Wang, J.; Yang, J.; Tang, Y.; Li, R.; Liang, G.; Sham, T.-K.; Sun, X. Surface aging at olivine $LiFePO_4$: A direct visual observation of iron dissolution and the protection role of nano-carbon coating. *Journal of Materials Chemistry A* 2013, *1*, 1579–1586, doi:10.1039/c2ta00521b.

107. Koltypin, M.; Aurbach, D.; Nazar, L.; Ellis, B. On the Stability of $LiFePO_4$ Olivine Cathodes under Various Conditions (Electrolyte Solutions, Temperatures). *Electrochemical and Solid-State Letters* 2007, *10*, A40, doi:10.1149/1.2403974.

108. Shkrob, I.A.; Kropf, A.J.; Marin, T.W.; Li, Y.; Poluektov, O.G.; Niklas, J.; Abraham, D.P. Manganese in Graphite Anode and Capacity Fade in Li Ion Batteries. *The Journal of Physical Chemistry C* 2014, *118*, 24335–24348, doi:10.1021/jp507833u.

109. Tsunekawa, H.; Tanimoto, a.S.; Marubayashi, R.; Fujita, M.; Kifune, K.; Sano, M. Capacity Fading of Graphite Electrodes Due to the Deposition of Manganese Ions on Them in Li-Ion Batteries. *Journal of The Electrochemical Society* 2002, *149*, A1326, doi:10.1149/1.1502686.

110. Pieczonka, N.P.W.; Liu, Z.; Lu, P.; Olson, K.L.; Moote, J.; Powell, B.R.; Kim, J.-H. Understanding Transition-Metal Dissolution Behavior in $LiNi_{0.5}Mn_{1.5}O_4$ High-Voltage Spinel for Lithium Ion Batteries. *The Journal of Physical Chemistry C* 2013, *117*, 15947–15957, doi:10.1021/jp405158m.

111. Saulnier, M.; Auclair, A.; Liang, G.; Schougaard, S.B. Manganese dissolution in lithium-ion positive electrode materials. *Solid State Ionics* 2016, *294*, 1–5, doi:10.1016/j.ssi.2016.06.007.

112. Kim, J.-H.; Pieczonka, N.P.W.; Li, Z.; Wu, Y.; Harris, S.; Powell, B.R. Understanding the capacity fading mechanism in $LiNi_{0.5}Mn_{1.5}O_4$/graphite Li-ion batteries. *Electrochimica Acta* 2013, *90*, 556–562, doi:10.1016/j.electacta.2012.12.069.

113. Buchberger, I.; Seidlmayer, S.; Pokharel, A.; Piana, M.; Hattendorff, J.; Kudejova, P.; Gilles, R.; Gasteiger, H.A. Aging Analysis of Graphite/$LiNi_{1/3}Mn_{1/3}Co_{1/3}O_2$ Cells Using XRD, PGAA, and AC Impedance. *Journal of The Electrochemical Society* 2015, *162*, A2737-A2746, doi:10.1149/2.0721514jes.

114. Bar-Tow, D. A Study of Highly Oriented Pyrolytic Graphite as a Model for the Graphite Anode in Li-Ion Batteries. *Journal of The Electrochemical Society* 1999, *146*, 824, doi:10.1149/1.1391688.

115. Wandt, J.; Freiberg, A.; Thomas, R.; Gorlin, Y.; Siebel, A.; Jung, R.; Gasteiger, H.A.; Tromp, M. Transition metal dissolution and deposition in Li-ion batteries investigated by operando X-ray absorption spectroscopy. *Journal of Materials Chemistry A* 2016, *4*, 18300–18305, doi:10.1039/c6ta08865a.

116. Starke, B.; Seidlmayer, S.; Schulz, M.; Dinter, A.; Revay, Z.; Gilles, R.; Pettinger, K.-H. Gas Evolution and Capacity Fading in $LiFe_xMn_{1-x}PO_4$ /Graphite Cells Studied by Neutron Imaging and Neutron Induced Prompt Gamma Activation Analysis. *Journal of The Electrochemical Society* 2017, *164*, A3943-A3948, doi:10.1149/2.0011802jes.

117. Röntgen, W.C. *Über Eine Neue Art von Strahlen;* Springer Berlin Heidelberg: Berlin, Heidelberg, 1949.

118. Hessenbruch, A. A brief history of x-rays. *Endeavour* 2002, *26*, 137–141, doi:10.1016/S0160-9327(02)01465-5.

119. "The Nobel Prize in Physics 1994". Available online: https://www.nobelprize.org/nobel_prizes/physics/laureates/1994/ (accessed on 08.03.2018).

120. Brockhouse, B.N. Slow neutron spectroscopy and the grand atlas of the physical world. *Reviews of Modern Physics* 1995, *67*, 735–751, doi:10.1103/RevModPhys.67.735.

121. Buyers, W.J.L. NEUTRON AND OTHER STORIES FROM CHALK RIVER. *Physics in Canada* 2000, *Vol. 56, No. 2*, 145–151.

122. Shull, C.G. Early development of neutron scattering. *Reviews of Modern Physics* 1995, *67*, 753–757, doi:10.1103/RevModPhys.67.753.

123. Rush, J. J.; Cappelletti R. L., "The NIST Center for Neutron Research: Over 40 Years Serving NIST/NBS and the Nation," NIST Special Publication 1120 (August 2011). Available online: http://ws680.nist.gov/publication/get_pdf.cfm?pub_id=908047 (accessed on 08.03.2018).

124. 40 Jahre Atom-Ei Garching. Available online: https://www.frm2.tum.de/fileadmin/w00bnv/www/Aktuelles___Medien/Broschueren/Sonstige/40Jahre_Atom-Ei.pdf (accessed on 08.03.2018).

125. Renaissance - The ILL Millenium Programme 2001 to 2009. Available online: https://www.ill.eu/fileadmin/user_upload/ILL/1_About_ILL/Documentation/Millenium_Brochure_2010.pdf (accessed on 08.03.2018).

126. Utsuro, M.; Ignatovich, V.K. *Neutron optics;* WILEY-VCH: Weinheim, 2010.

127. Seiler, P.; Martinoni, B.; Dunitz, J.D. Can X-ray diffraction distinguish between protium and deuterium atoms? *Nature* 1984, *309*, 435–438, doi:10.1038/309435a0.

128. Petrov, Y.V.; Shlyakhter, A.I. The Distribution of Thermal Neutron Cross Sections. *Nuclear Science and Engineering* 2017, *77*, 157–167, doi:10.13182/NSE81-A21350.

129. Chatake, T.; Fujiwara, S. A technique for determining the deuterium/hydrogen contrast map in neutron macromolecular crystallography. *Acta crystallographica. Section D, Structural biology* 2016, *72*, 71–82, doi:10.1107/S2059798315021269.

130. Pynn, R. Neutron Scattering - A Non-destructive Microscope for Seeing Inside Matter. In *Neutron Applications in Earth, Energy and Environmental Sciences*; Anderson, I.S., Hurd, A.J., McGreevy, R.L., Liang, L., Rinaldi, R., Schober, H., Eds.; Springer US: Boston, MA, 2009; pp 15–36.

131. Jones, P. G.: Neutronenbeugung. Available online: https://www.gdch.de/fileadmin/downloads/Netzwerk_und_Strukturen/Fachgruppen/Analytische_Chemie/chemkrist/jones_4.pdf (accessed on 14.03.2018).

132. Lexikon der Wissenschaften: Atomstreufaktor. Available online: http://www.spektrum.de/lexikon/geowissenschaften/atomstreufaktor/1086 (accessed on 14.03.2018).

133. Castellanos, M.M.; McAuley, A.; Curtis, J.E. Investigating Structure and Dynamics of Proteins in Amorphous Phases Using Neutron Scattering.

*Computational and structural biotechnology journal* 2017, *15*, 117–130, doi:10.1016/j.csbj.2016.12.004.

134. Sears, V.F. Neutron scattering lengths and cross sections. *Neutron News* 2006, *3*, 26–37, doi:10.1080/10448639208218770.

135. Ankner, J.F.; Heller, W.T.; Herwig, K.W.; Meilleur, F.; Myles, D.A.A. Neutron scattering techniques and applications in structural biology. *Current protocols in protein science* 2013, *Chapter 17*, Unit17.16, doi:10.1002/0471140864.ps1716s72.

136. McMaster, W.H.; Kerr Del Grande, N.; Mallett, J.H.; Hubbell, J.H. Compilation of x-ray cross sections UCRL-50174, sections I, II revision 1, III, IV. *Atomic Data and Nuclear Data Tables* 1970, *8*, 443–444, doi:10.1016/S0092-640X(70)80026-2.

137. Birkholz, M.; Fewster, P.F. *Thin film analysis by X-Ray scattering*, 2nd reprint; WILEY-VCH: Weinheim, 2009.

138. Balagurov, A.M.; Bobrikov, I.A.; Samoylova, N.Y.; Drozhzhin, O.A.; Antipov, E.V. Neutron scattering for analysis of processes in lithium-ion batteries. *Russian Chemical Reviews* 2014, *83*, 1120–1134, doi:10.1070/RCR4473.

139. Etacheri, V.; Marom, R.; Elazari, R.; Salitra, G.; Aurbach, D. Challenges in the development of advanced Li-ion batteries: A review. *Energy & Environmental Science* 2011, *4*, 3243, doi:10.1039/c1ee01598b.

140. Sharma, N.; Peterson, V.K.; Elcombe, M.M.; Avdeev, M.; Studer, A.J.; Blagojevic, N.; Yusoff, R.; Kamarulzaman, N. Structural changes in a commercial lithium-ion battery during electrochemical cycling: An in situ neutron diffraction study. *Journal of Power Sources* 2010, *195*, 8258–8266, doi:10.1016/j.jpowsour.2010.06.114.

141. Zinth, V.; Lüders, C. von; Wilhelm, J.; Erhard, S.V.; Hofmann, M.; Seidlmayer, S.; Rebelo-Kornmeier, J.; Gan, W.; Jossen, A.; Gilles, R. Inhomogeneity and relaxation phenomena in the graphite anode of a lithium-ion battery probed by in situ neutron diffraction. *Journal of Power Sources* 2017, *361*, 54–60, doi:10.1016/j.jpowsour.2017.06.060.

142. Lüders, C.v.; Zinth, V.; Erhard, S.V.; Osswald, P.J.; Hofmann, M.; Gilles, R.; Jossen, A. Lithium plating in lithium-ion batteries investigated by voltage relaxation and in situ neutron diffraction. *Journal of Power Sources* 2017, *342*, 17–23, doi:10.1016/j.jpowsour.2016.12.032.

143. Zinth, V.; Lüders, C. von; Hofmann, M.; Hattendorff, J.; Buchberger, I.; Erhard, S.; Rebelo-Kornmeier, J.; Jossen, A.; Gilles, R. Lithium plating in lithium-ion batteries at sub-ambient temperatures investigated by in situ

neutron diffraction. *Journal of Power Sources* 2014, *271*, 152–159, doi:10.1016/j.jpowsour.2014.07.168.

144. Aurbach, D. A short review of failure mechanisms of lithium metal and lithiated graphite anodes in liquid electrolyte solutions. *Solid State Ionics* 2002, *148*, 405–416, doi:10.1016/S0167-2738(02)00080-2.
145. Feng, X.; Ouyang, M.; Liu, X.; Lu, L.; Xia, Y.; He, X. Thermal runaway mechanism of lithium ion battery for electric vehicles: A review. *Energy Storage Materials* 2018, *10*, 246–267, doi:10.1016/j.ensm.2017.05.013.
146. Finegan, D.P.; Scheel, M.; Robinson, J.B.; Tjaden, B.; Hunt, I.; Mason, T.J.; Millichamp, J.; Di M., M.; Offer, G.J.; Hinds, G.*; et al.* In-operando high-speed tomography of lithium-ion batteries during thermal runaway. *Nature communications* 2015, *6*, 6924, doi:10.1038/ncomms7924.
147. Smart, M.C.; Ratnakumar, B.V. Effects of Electrolyte Composition on Lithium Plating in Lithium-Ion Cells. *Journal of The Electrochemical Society* 2011, *158*, A379, doi:10.1149/1.3544439.
148. Zhao, E.; Fang, L.; Chen, M.; Chen, D.; Huang, Q.; Hu, Z.; Yan, Q.-b.; Wu, M.; Xiao, X. New insight into Li/Ni disorder in layered cathode materials for lithium ion batteries: A joint study of neutron diffraction, electrochemical kinetic analysis and first-principles calculations. *Journal of Materials Chemistry A* 2017, *5*, 1679–1686, doi:10.1039/c6ta08448f.
149. Samarasingha, P.B.; Andersen, N.H.; Sørby, M.H.; Kumar, S.; Nilsen, O.; Fjellvåg, H. Neutron diffraction and Raman analysis of $LiMn_{1.5}Ni_{0.5}O_4$ spinel type oxides for use as lithium ion battery cathode and their capacity enhancements. *Solid State Ionics* 2016, *284*, 28–36, doi:10.1016/j.ssi.2015.11.018.
150. Paul, N.; Wandt, J.; Seidlmayer, S.; Schebesta, S.; Mühlbauer, M.J.; Dolotko, O.; Gasteiger, H.A.; Gilles, R. Aging behavior of lithium iron phosphate based 18650-type cells studied by in situ neutron diffraction. *Journal of Power Sources* 2017, *345*, 85–96, doi:10.1016/j.jpowsour.2017.01.134.
151. Brenizer, J.S. A Review of Significant Advances in Neutron Imaging from Conception to the Present. *Physics Procedia* 2013, *43*, 10–20, doi:10.1016/j.phpro.2013.03.002.
152. Schulz, M.L. Radiography with polarised neutrons. München, Techn. Univ., Diss., 2010.
153. McGregor, D.S.; Hammig, M.D.; Yang, Y.-H.; Gersch, H.K.; Klann, R.T. Design considerations for thin film coated semiconductor thermal neutron detectors—I: Basics regarding alpha particle emitting neutron reactive films. *Nuclear Instruments and Methods in Physics Research Section A: Accelerators,*

*Spectrometers, Detectors and Associated Equipment* 2003, *500*, 272–308, doi:10.1016/S0168-9002(02)02078-8.

154. Kardjilov, N.; Manke, I.; Hilger, A.; Strobl, M.; Banhart, J. Neutron imaging in materials science. *Materials Today* 2011, *14*, 248–256, doi:10.1016/S1369-7021(11)70139-0.

155. Pleinert, H.; Lehmann, E.; Körner, S. Design of a new CCD-camera neutron radiography detector. *Nuclear Instruments and Methods in Physics Research Section A: Accelerators, Spectrometers, Detectors and Associated Equipment* 1997, *399*, 382–390, doi:10.1016/S0168-9002(97)00944-3.

156. Lehmann, E.H.; Vontobel, P.; Frei, G.; Brönnimann, C. Neutron imaging - detector options and practical results. *Nuclear Instruments and Methods in Physics Research Section A: Accelerators, Spectrometers, Detectors and Associated Equipment* 2004, *531*, 228–237, doi:10.1016/j.nima.2004.06.010.

157. Knoche, T.; Reinhart, G. Electrolyte Filling of Large-Scale Lithium-Ion Batteries: Main Influences and Challenges for Production Technology. *Applied Mechanics and Materials* 2015, *794*, 11–18, doi:10.4028/www.scientific.net/AMM.794.11.

158. Jung, Y.S.; Cavanagh, A.S.; Gedvilas, L.; Widjonarko, N.E.; Scott, I.D.; Lee, S.-H.; Kim, G.-H.; George, S.M.; Dillon, A.C. Improved Functionality of Lithium-Ion Batteries Enabled by Atomic Layer Deposition on the Porous Microstructure of Polymer Separators and Coating Electrodes. *Advanced Energy Materials* 2012, *2*, 1022–1027, doi:10.1002/aenm.201100750.

159. Knoche, T.; Zinth, V.; Schulz, M.; Schnell, J.; Gilles, R.; Reinhart, G. In situ visualization of the electrolyte solvent filling process by neutron radiography. *Journal of Power Sources* 2016, *331*, 267–276, doi:10.1016/j.jpowsour.2016.09.037.

160. Zhang, S.S. Insight into the Gassing Problem of Li-ion Battery. *Frontiers in Energy Research* 2014, *2*, 8694, doi:10.3389/fenrg.2014.00059.

161. Kong, W.; Li, H.; Huang, X.; Chen, L. Gas evolution behaviors for several cathode materials in lithium-ion batteries. *Journal of Power Sources* 2005, *142*, 285–291, doi:10.1016/j.jpowsour.2004.10.008.

162. Berkes, B.B.; Schiele, A.; Sommer, H.; Brezesinski, T.; Janek, J. On the gassing behavior of lithium-ion batteries with NCM523 cathodes. *Journal of Solid State Electrochemistry* 2016, *20*, 2961–2967, doi:10.1007/s10008-016-3362-9.

163. Bernhard, R.; Meini, S.; Gasteiger, H.A. On-Line Electrochemical Mass Spectrometry Investigations on the Gassing Behavior of $Li_4Ti_5O_{12}$ Electrodes

and Its Origins. *Journal of The Electrochemical Society* 2014, *161*, A497-A505, doi:10.1149/2.013404jes.

164. Lv, W.; Gu, J.; Niu, Y.; Wen, K.; He, W. Review - Gassing Mechanism and Suppressing Solutions in $Li_4Ti_5O_{12}$ -Based Lithium-Ion Batteries. *Journal of The Electrochemical Society* 2017, *164*, A2213-A2224, doi:10.1149/2.0031712jes.

165. Michalak, B.; Sommer, H.; Mannes, D.; Kaestner, A.; Brezesinski, T.; Janek, J. Gas Evolution in Operating Lithium-Ion Batteries Studied In Situ by Neutron Imaging. *Scientific reports* 2015, *5*, 15627, doi:10.1038/srep15627.

166. Michalak, B.; Berkes, B.B.; Sommer, H.; Bergfeldt, T.; Brezesinski, T.; Janek, J. Gas Evolution in $LiNi_{0.5}Mn_{1.5}O_4$/Graphite Cells Studied In Operando by a Combination of Differential Electrochemical Mass Spectrometry, Neutron Imaging, and Pressure Measurements. *Analytical chemistry* 2016, *88*, 2877–2883, doi:10.1021/acs.analchem.5b04696.

167. Goers, D.; Holzapfel, M.; Scheifele, W.; Lehmann, E.; Vontobel, P.; Novák, P. In situ neutron radiography of lithium-ion batteries: The gas evolution on graphite electrodes during the charging. *Journal of Power Sources* 2004, *130*, 221–226, doi:10.1016/j.jpowsour.2003.11.065.

168. Takai, S. Diffusion coefficient measurement of lithium ion in sintered $Li_{1.33}$ $Ti_{1.67}$ $O_4$ by means of neutron radiography. *Solid State Ionics* 1999, *123*, 165–172, doi:10.1016/S0167-2738(99)00095-8.

169. Esaka, T. Analysis of lithium ion distribution in electrolyzed $Li_{1.33}Ti_{1.67}O_4$ by Neutron Computed Tomography. *Solid State Ionics* 2002, *147*, 107–114, doi:10.1016/S0167-2738(01)01039-6.

170. Anderson, C.D. The Positive Electron. *Physical Review* 1933, *43*, 491–494, doi:10.1103/PhysRev.43.491.

171. Hugenschmidt, C.; Löwe, B.; Mayer, J.; Piochacz, C.; Pikart, P.; Repper, R.; Stadlbauer, M.; Schreckenbach, K. Unprecedented intensity of a low-energy positron beam. *Nuclear Instruments and Methods in Physics Research Section A: Accelerators, Spectrometers, Detectors and Associated Equipment* 2008, *593*, 616–618, doi:10.1016/j.nima.2008.05.038.

172. Hugenschmidt, C.; Piochacz, C. NEPOMUC: Neutron induced positron source Munich. *Journal of large-scale research facilities JLSRF* 2015, *1, doi:*10.17815/jlsrf-1-49.

173. Seidlmayer, S.; Buchberger, I.; Reiner, M.; Gigl, T.; Gilles, R.; Gasteiger, H.A.; Hugenschmidt, C. First-cycle defect evolution of $Li_{1-x}Ni_{1/3}Mn_{1/3}Co_{1/3}O_2$ lithium ion battery electrodes investigated by positron annihilation spectroscopy. *Journal of Power Sources* **2016**, *336*, 224–230, doi:10.1016/j.jpowsour.2016.10.050.

174. Parz, P.; Fuchsbichler, B.; Koller, S.; Bitschnau, B.; Mautner, F.-A.; Puff, W.; Würschum, R. Charging-induced defect formation in $Li_xCoO_2$ battery cathodes studied by positron annihilation spectroscopy. *Applied Physics Letters* 2013, *102*, 151901, doi:10.1063/1.4801998.
175. Barbiellini, B.; Kuriplach, J. Advanced characterization of lithium battery materials with positrons. *Journal of Physics: Conference Series* 2017, *791*, 12016, doi:10.1088/1742-6596/791/1/012016.
176. Bücherl, T.; Kutlar, E.; Gostomski, C.L.v.; Calzada, E.; Pfister, G.; Koch, D. Radiography and tomography with fast neutrons at the FRM-II -a status report. *Applied radiation and isotopes : including data, instrumentation and methods for use in agriculture, industry and medicine* 2004, *61*, 537–540, doi:10.1016/j.apradiso.2004.03.095.
177. Böning, K.; Gläser, W.; Steichele, E.; Waschkowski, W. Aktuelles Thema: Die neue Neutronenquelle Forschungsreaktor München II. *Physik Journal* 1994, *50*, 947–949, doi:10.1002/phbl.19940501011.
178. Pro und Contra: Soll der in Garching geplante Forschungsreaktor FRM-II mit hochangereichertem Uran betrieben werden? *Phys. Bl.* 1994, *50*, 621–625, doi:10.1002/phbl.19940500705.
179. Axmann, A.; Böning, K.; Rottmann, M. FRM-II: The new German research reactor. *Nuclear Engineering and Design* 1997, *178*, 127–133, doi:10.1016/S0029-5493(97)00215-X.
180. Röhrmoser, A. Core model of new German neutron source FRM II. *Nuclear Engineering and Design* 2010, *240*, 1417–1432, doi:10.1016/j.nucengdes.2010.02.011.
181. Teruel, F.E.; Rizwan-uddin. An innovative research reactor design. *Nuclear Engineering and Design* 2009, *239*, 395–407, doi:10.1016/j.nucengdes.2008.10.025.
182. Petry, W.; Neuhaus, J. Neutronen nach Maß: Die Forschungsneutronenquelle Heinz Maier-Leibnitz bietet brillante Neutronenstrahlen für Wissenschaft, Technik und Medizin. *Physik Journal* 2007, *07*, 31–37.
183. Böning, K.; Gläser, W.; Hennings, U.; Streichele, E. Neutronenquelle FRM-II. *Atomwirtschaft, Atomtechnik* 1993, *38(1)*, 61–65.
184. Hoelzel, M.; Senyshyn, A.; Dolotko, O. SPODI: High resolution powder diffractometer. *Journal of large-scale research facilities JLSRF* 2015, *1, doi:*10.17815/jlsrf-1-24.
185. Hoelzel, M.; Senyshyn, A.; Juenke, N.; Boysen, H.; Schmahl, W.; Fuess, H. High-resolution neutron powder diffractometer SPODI at research reactor FRM II. *Nuclear Instruments and Methods in Physics Research Section A:*

*Accelerators, Spectrometers, Detectors and Associated Equipment* 2012, *667*, 32–37, doi:10.1016/j.nima.2011.11.070.

186. Gilles, R.; Hoelzel, M.; Schlapp, M.; Elf, F.; Krimmer, B.; Boysen, H.; Fuess, H. First test measurements at the new structure powder diffractometer (SPODI) at the FRM-II. *Zeitschrift für Kristallographie Supplements* 2006, *2006*, 183–188, doi:10.1524/zksu.2006.suppl_23.183.
187. Schulz, M.; Schillinger, B. ANTARES: Cold neutron radiography and tomography facility. *Journal of large-scale research facilities JLSRF* 2015, *1, doi:*10.17815/jlsrf-1-42.
188. Schillinger, B.; Calzada, E.; Grünauer, F.; Steichele, E. The design of the neutron radiography and tomography facility at the new research reactor FRM-II at Technical University Munich. *Applied radiation and isotopes : including data, instrumentation and methods for use in agriculture, industry and medicine* 2004, *61*, 653–657, doi:10.1016/j.apradiso.2004.03.091.
189. Calzada, E.; Gruenauer, F.; Mühlbauer, M.; Schillinger, B.; Schulz, M. New design for the ANTARES-II facility for neutron imaging at FRM II. *Nuclear Instruments and Methods in Physics Research Section A: Accelerators, Spectrometers, Detectors and Associated Equipment* 2009, *605*, 50–53, doi:10.1016/j.nima.2009.01.192.
190. Revay, Z. PGAA: Prompt gamma and in-beam neutron activation analysis facility. *Journal of large-scale research facilities JLSRF* 2015, *1, doi:*10.17815/jlsrf-1-46.
191. Introduction to Dispersion Technology with the DISPERMAT® Dissolver. Available online: http://www.vma-getzmann.com/english/dispersing_&_grinding_know-how/dispersing_with_dissolvers/dispersing_with_dissolvers_0_935_987_1809.html (accessed on 28.02.2018).
192. Lorentzen, T. *Introduction to Characterization of Residual Stress by Neutron Diffraction;* CRC Press: London, 2004.
193. Khidirov, I. *Neutron Diffraction;* Intech: Rijeka, Croatia, 2012.

# List of Figures

# Acknowledgement

This work has been carried out in collaboration between the University of Applied Sciences Landshut and the Chair of Technical Electrochemistry at the Technical University of Munich.

I gratefully acknowledge and express my appreciation to Prof. Dr. Hubert Gasteiger and Prof. Dr. Karl-Heinz Pettinger for giving me the opportunity to work on this project and their excellent supervision. They gave me the freedom and time to realize ideas and evolve the project according to my interests, and provided me with the unique chance to participate in many international research activities.

I express my gratitude to Dr. habil. Ralph Gilles for the successful cooperation in neutron experiments at FRM II and his valuable help and advice during the whole project.

My special thanks go to Dr. Stefan Seidlmayer for his substantial and dedicated support regarding experiments and data evaluation, but also for his patience and numerous helpful discussions and explanations.

Furthermore, I would like to thank my working partners and colleagues Alexander Dinter, Christina Toigo, Andrea Sammereier, Martin Frankenberger, Dr. Michael Schulz, Dr. Zsolt Revay, Dr. Sebastian Jankowsky and Dr. Oleksandr Dolotko for their contribution to the success of this work.

I conclude by thanking my family for unconditional support at any time and in any situation.